Preprint submitted to EarthArXiv of paper submitted to *Earth & Planetary Science Letters* for peer review

June 30, 2023

Cosmogenic nuclide dating conundrum for retreat of the Laurentide Ice Sheet and the critical roles of geomagnetic and heliomagnetic modulation of cosmic ray flux

Dennis V. Kent <*dvk@ldeo.columbia.edu*>[1,2]

Luca Lanci <*luca.lanci@uniurb.it*>[3]

Dorothy M. Peteet <*peteet@ldeo.columbia.edu*>[1,4]

[1]Lamont-Doherty Earth Observatory of Columbia University, Palisades, NY 10968

[2]Earth & Planetary Sciences, Rutgers University, Piscataway, NJ 08854

[3]Department of Pure and Applied Science, University of Urbino, Urbino, Italy

[4]NASA Goddard Institute for Space Studies, New York, NY 10025

Rev.1: add Section S2 to Supplementary Information, edit Acknowledgments.

Cosmogenic nuclide dating conundrum for retreat of the Laurentide Ice Sheet and the critical roles of geomagnetic and heliomagnetic modulation of cosmic ray flux

Dennis V. Kent[1,2]
Luca Lanci[3]
Dorothy M. Peteet[1,4]

[1]Lamont-Doherty Earth Observatory of Columbia University, Palisades, NY 10968
[2]Earth & Planetary Sciences, Rutgers University, Piscataway, NJ 08854
[3]Department of Pure and Applied Science, University of Urbino, Urbino, Italy
[4]NASA Goddard Institute for Space Studies, New York, NY 10025

dvk@ldeo.columbia.edu; *luca.lanci@uniurb.it*; *peteet@ldeo.columbia.edu*

Abstract

What we regard as anomalously old ^{10}Be exposure dates reported from the terminal moraine of the Laurentide Ice Sheet (LIS) in northeastern North America, such as recently published for Allamuchy NJ, ostensibly point to the start of deglaciation at 25 thousand calendar years before present (cal. ka). These dates are well within the conventional age span of the Last Glacial Maximum (LGM) and are in stark contrast with published ^{14}C accelerator mass spectrometry (AMS) dates for earliest terrestrial plant macrofossils found in LIS deglacial clay deposits that range back to only ~16 cal. ka, which more plausibly coincide with the known timing of the glacio-eustatic rise and meltwater discharge to the North Atlantic and Gulf of Mexico that mark the demise of the LGM in the marine record. To explore possible explanations for this inconsistency, we first employed a statistical model of the geomagnetic field that includes secular variation with nondipole terms and can be applied globally. The model results in a decrease in the magnetic shielding factor by about 10% at mid-latitudes compared to oft-used geomagnetic scaling schemes. However, the time-integrated axial dipole moment estimated separately suggests little overall change in average shielding since about 20 cal. ka. This seems to leave cosmic ray flux modulated by a time-varying heliomagnetic field linked to sunspot activity as an underestimated factor in widely used ^{10}Be exposure age calculators. If generally

biased by about 23% higher compared to modern levels as reported for the past 9.4 cal. ka, the elevated high cosmic ray flux would make ^{10}Be reference production rates proportionately higher, to about 5.5 at/g/y at sea level-high latitude, and reduce exposure ages to about 3/4 of those that have been previously calculated for LGM and younger rocks (to less than 20 cal. ka in the case of Allamuchy). Varying but generally higher solar modulation will require reevaluation of cosmogenic exposure dates in general, as in the case of Allamuchy, that would allow improved synchronization of marine and terrestrial records of glaciation. Other test cases can result in improved GIA deglaciation models and alternative estimates of effects of shielding in ice-flow models.

1. Introduction

There are widely divergent published results from cosmogenic surface exposure dating and radiocarbon chronologies for the retreat of the Laurentide ice sheet (LIS) from the Last Glacial Maximum (LGM) in northeastern North America (**Fig. 1**). Recession of the southeastern lobe of the LIS was placed at around 25 cal. ka (calendar kilo-annum or thousands of years ago) according to ^{10}Be measurements on glacial boulders associated with terminal moraines in New England and ostensibly supported by ^{14}C bulk sediment dates ranging from ~22 to 27 cal. ka on deglacial sediments in the region (Balco et al., 2009; Balco and Schaefer, 2006; Balco et al., 2002). However, Peteet et al. (2012) soon afterwards reported calibrated ^{14}C accelerator mass spectrometry (AMS) dates on terrestrial plant macrofossils in earliest deglacial sediments in the region that range back to only ~16 cal. ka. The younger timing was seen as much more compatible with the well-dated sea level record, which implied that melting of the LIS, the largest variable continental ice volume for the LGM (circa. 16–29 cal. ka) and equivalent to 70 to 80 m of the ~120 m sea level drop that characterizes it (Clark and Mix, 2002; Tarasov et al., 2012), did not sensibly proceed until around 20 cal. ka and not in earnest until about 16 cal. ka (**Fig. 2**).

Nonetheless, a recent ^{10}Be exposure age study (Corbett et al., 2017) that builds on unpublished but widely cited thesis work (Larsen, 1996) on glacial boulders and pavements associated with the terminal moraine in Allamuchy Forest and vicinity in northern New Jersey (NJ) (**Fig. 1**) also reported an exposure age of 25.2±2.1 cal. ka. The ^{10}Be exposure ages of ~25 cal. ka taken at face value would imply that the southeastern lobe of the LIS started to retreat during maximum ice volume well within the LGM as denoted by low global sea-level (**Fig. 2**). As pointed out by Peteet et al. (2012), this would also imply an extraordinarily long delay of 9,000 years (from 25 cal. ka until 16 cal. ka) before introduction of vegetation on the deglaciated landscape. Such an extended delay in temperate latitudes does not seem plausible (Jones and Henry, 2003; Matthews, 1992) because trees today grow in close proximity to (and even on debris-covered) glaciers in southern Alaska including on permafrost (Fickert et al., 2007) with rapid primary succession by plants following deglaciation in decades (Chapin et al., 1994; Cooper, 1923). The oldest ^{14}C AMS-dated terrestrial plant macrofossils found thus far occur in clays of less than 5% organic content that argue for deposition with glacial meltwater during earliest ice retreat.

The broader conflict between old ^{14}C bulk sediment dates and younger ^{14}C AMS dates on terrestrial plant macrofossils in the same clays of deglaciation bog/limnic sequences associated with the LIS terminal moraine is systemic and regional in scope (**Fig. 3**). For example, reliance is still placed (Corbett et al., 2017) on previously rejected ^{14}C bulk sediment dates of 27.2±1.4 cal. ka at Budd Lake, NJ (unpublished thesis of Harmon, 1968) and 25.8±1.6 cal. ka in a contorted section of the Harbor Hill moraine in Port Washington on Long Island, New York (Sirkin and Stuckenrath, 1980). These dates are from the same terminal moraine associated with published ^{14}C AMS dates on first appearance of tundra plants from basal silts/clays of 14.4 ±0.4 cal. ka at Tannersville just to the west of Budd Lake and 14.6±0.3 cal. ka at High Rock just to the east (Peteet et al., 2012) (**Fig. 4**). More pertinently, Corbett et al. (2017) cite evidence from controversial ^{14}C bulk sediment dates of 22.2 and 22.5 cal. ka from nearby Francis Lake (unpublished thesis of Cotter, 1983; but see opposing view by Karrow et al., 1986) in support of the ^{10}Be exposure age of 25.2±2.1 cal. ka that was obtained from glacial pavement and boulders at nearby Allamuchy Forest and environs. Yet at Allamuchy Pond the same litho- and biostratigraphy is recorded as at Francis Lake only 6 km to the west where *Dryas* and willow leaves screened from basal clays in the basal herb zone transition are ^{14}C AMS dated at 14.4 ±0.8 cal. ka (Peteet et al., 2012; Peteet et al., 1993).

The requisite usage of terrestrial macrofossils for ^{14}C AMS dating in basal clays/silts for timing of deglaciation versus ^{14}C dates on bulk sediment, which is apt to be contaminated by older carbon in the landscape, is widely acknowledged (e.g., Birks, 1993; Curry et al., 2010; Gaglioti et al., 2014; Grimm et al., 2009; Hajdas et al., 1993; Peteet et al., 1993; Peteet and

Mann, 1994; Peteet et al., 1990; Thompson et al., 2017; Zimmerman and Wahl, 2020). Moreover, usage of terrestrial rather than aquatic plant macrofossils, which tend to give variably older ^{14}C dates (MacDonald et al., 1987), is essential for radiocarbon dating accuracy in these environments (Birks, 2002; Marty and Myrbo, 2014).

Recently updated compilations (Dalton et al., 2020; Wickert et al., 2023) that include ^{14}C AMS terrestrial plant macrofossil dates and reject the earlier bulk dating used by Dyke et al. (2003) indicate that the southern Laurentide margin was at LGM extent from 26.0 to 18.7 cal. ka (**Fig. 1**). This timing is in tempo with the global sea level record (**Fig. 2**) and with independent evidence that meltwater to the North Atlantic was minimal prior to 18.5 cal. ka (Keigwin et al., 1991) and started by 16.1 cal. ka in the Gulf of Mexico (Flower et al., 2004). The 25 cal. ka ^{10}Be exposure age for the terminal moraine in NJ (Corbett et al., 2017) thus appears anomalously old even in this broader context and despite the continued usage of old ^{14}C bulk dates for support (Stanford et al., 2020).

2. ^{10}Be production and surface exposure dating

Cosmogenic exposure dating is a long-established technique of more than 30 years and is based on measurements of the concentration of a cosmogenic nuclide, in this case, ^{10}Be produced in quartz in natural rock surfaces (Gosse and Phillips, 2001; Lal, 1991). The basic assumption is that the flux of highly energetic charged particles (~90% protons, ~10% helium nuclei) constituting galactic cosmic rays is constant over long time scales (Aab and others, 2017) although modulated in Earth's space environment by a varying solar magnetic field (Steinhilber et al., 2012). Production of ^{10}Be takes place overwhelmingly by high-energy spallation from secondary particles produced in the atmosphere and occurs within centimeters of the rock surface with only ~2% by interactions with deeper penetrating muons (Balco, 2017). Production rates depend strongly on the site altitude, an approximation of atmospheric pressure or weight but in the case of spallation the cosmogenic production is also modulated by the local geometry and magnitude of the time-varying geomagnetic field to about 60° in magnetic latitudes (74° in magnetic inclination), poleward of which the geomagnetic dependency becomes negligible.

A variety of scaling schemes have been used to normalize ^{10}Be production at a given site to sea level and high latitude (SLHL). Five scaling schemes (St, De, Du, Li, Lm) are in the various versions of the first online exposure age calculator (v2, v2.2, v2.3; Balco et al., 2008) and two additional schemes (LSDn, LSD) for a total of seven in the CRONUS-Earth effort (Marrero et al., 2016; Phillips et al., 2016a). The reported differences in applications amongst the various scaling schemes tend to be small and are often averaged although there remain "*substantial unresolved difficulties in modeling cosmogenic nuclide production and the calibration of production rates*" (Borchers et al., 2016).

The number of scaling schemes has been mercifully reduced to only three in the recent version (v3) of the widely used 'online exposure age calculator formerly known as the CRONUS-Earth online exposure age calculator' (http://hess.ess.washington.edu/; https://cosmognosis.wordpress.com/2016/08/01/let-a-hundred-flowers-bloom/). Scheme St continues from the initial version of the online exposure age calculator and is based on the latitude-altitude scaling factors of (Lal, 1991) recast in terms of atmospheric pressure by (Stone, 2000) and for the geomagnetic latitude of the present-day field. Scheme Lm is basically scheme St with a time-varying geomagnetic field intensity model, which according to what documentation is available online for v3 (https://sites.google.com/a/bgc.org/v3docs/), is now a spherical harmonic analysis (SHA) of the geomagnetic field for the past 14 cal. ka (SHA.DIF.14k; Pavón-Carrasco et al., 2014) and a geocentric axial dipole (GAD) field with a prescribed time-varying dipole moment model for earlier periods. A third scheme, LSDn, is a nuclide-dependent variant (Phillips et al., 2016a) of what is described as a physics-based analytical framework for *in situ* cosmogenic nuclide production (Lifton et al., 2014). LSDn apparently uses the same geomagnetic field model as scheme Lm with look-up tables of precalculated scaling factors for the forward integrations. We could not readily access these tables and instead focus on simple numerical experiments with the longstanding St-Lm schemes based on empirical data and the Desilets-Dunai-Lifton (DeDuLi) schemes that LSDn seems similar to and utilize particle ray trajectory tracing to calculate effective vertical cutoff rigidities as a geomagnetic cutoff parameter, a common parameterization of cosmic ray intensity measurements.

2.1 St and Rc-based scaling schemes

We calculate spallation rate factors for scheme St from scaling equation coefficients in Stone (2000) normalized to the value at 60° latitude and a standard sea level pressure. The DeDuLi schemes are based on analytical estimates of the effective vertical cutoff rigidity, *Rc* (here using Equation 2 of Lifton et al. (2014) for consistency). These and other relevant functions are included in **Section S1** as routines for heuristic purposes in the R programming language (R_Core_Team, 2018) .

The altitude scaling factor for spallation reactions (Eq. 7 in (Desilets et al., 2006)) as given in terms of R_c and atmospheric depth or weight (*x*) relative to sea level (1033 g/cm^2, equal to standard atmospheric pressure of 1023.15 hPa) agrees well with the original empirical altitude scaling factor for the Lal/Stone St scheme from sea level to about 800 hPa (~2000 m altitude) but then the St and R_c-based scaling factors diverge with decreasing atmospheric pressure (higher altitude) (**Fig. 5A**). The scaling factor for latitude depends on the geomagnetic field model and has more variants than for altitude. The Lal/Stone St scheme has numerically larger scaling factors at any given latitude, ranging albeit not very regularly from almost 0.6 at the equator to 1.0 at 60° latitude poleward of which cosmogenic production rates become essentially independent of the geomagnetic latitude (Elsasser et al., 1956; Gosse and Phillips, 2001; Lifton et al., 2014) (**Fig. 5B**). The St scaling factor is cast in terms of geomagnetic latitude (presumably equivalent to geographic latitude in this context although that is not entirely clear) to organize and model the empirical cosmogenic data, a common practice in all scaling schemes, rather than the directly observable local geomagnetic inclination (as in Dunai, 2000; see also informative Comment and Reply of Desilets et al. (2001) and Dunai (2001))

For a geomagnetic dipole field of comparable modern magnetic moment (~80 ZAm^2), geomagnetic shielding for spallation reactions expressed in terms of *Rc* can then be used to calculate a latitude scaling factor ($f(Rc)$) using Eq. 6 with Dorman function in Desilets et al. (2006). The $f(Rc)$ factor at sea level takes the canonical sigmoidal form plotted for a stationary GAD field (**Fig. 5B**) and varies from ~0.54 at the equator to 1.0 at the 'knee' at 60° and higher latitudes. Other geomagnetic models have similar sigmoidal curves and are discussed below. The grand scaling factor, *F*, is then the product of the latitude and altitude scaling factors ($F(Rc,x) = f(Rc)\, f(x)$), which can be used to estimate the ^{10}Be production rate ($P(Rc,x)$) at a sample site relative to the production rate (P_0) at a SLHL calibration site using Eq. 8 in Desilets et al. (2006): $P(Rc,x) = F * P_0$.

2.2 Rc and dipole wobble

The SHA-DIF-14k model (Pavón-Carrasco et al., 2014), which is apparently now used in scheme Lm as well as LSDn in version v3 of the online calculator, is inherently limited by the inhomogeneous distribution of available archeomagnetic and volcanic paleomagnetic data: 97% of the total in this analysis are located in the Northern Hemisphere and 83% of the total are from 3 cal. ka to present. The spherical harmonic model is nonetheless sufficient to calculate virtual geomagnetic poles (VGPs) from estimates of the dipole (g^0_1, g^1_1 and h^1_1) coefficients that are provided at 50-year intervals since 14 cal. ka (data listings available in the Earth Ref Digital Archive at http://earthref.org/ERDA/1897/). The overall mean VGP pole position is located at 89.3°N 337.0°E (n= 279, angular standard deviation (ASD) = 7.6°, precision parameter (K) = 118, and radius of circle of 95% confidence (A95) = 0.8°), which is not significantly different from the geographic axis despite the very tight grouping of the VGPs. This close correspondence confirms that the GAD provides an appropriate fit to the geomagnetic field averaged over the past 14 cal. ka, and importantly, even within just 2 cal. ka according to Pavón-Carrasco et al. (2014). The average *Rc* will thus be essentially the same whether calculated with respect to the latitude from the mean VGP pole or with respect to the geographic axis for any site; nonetheless, *Rc* averaged from constituent VGP distributions will tend to be sensibly different because of nonlinearity in the relationship of *Rc* and latitude. The VGP dispersion can be regarded as a proxy for the effect of the dipole wobble component of secular variation of the geomagnetic field on *Rc*. The small dispersion of VGP poles from SHA-DIF-14k (K=118), however, hardly captures the full range of secular variation (as discussed below) and thus differs from the singular GAD pattern by only a few percent in mid-latitudes (**Fig. 5B**).

2.3 Rc and a statistical geomagnetic field model

A more generalized approach to latitude scaling is to use a statistical model of the geomagnetic field that includes the full range of spherical harmonic contributions to the secular variation and that is also conveniently applicable over time scales of arbitrary duration from thousands to even millions of years ago. A candidate model is TK03 (Tauxe and Kent, 2004) where the geomagnetic field is treated as a Giant Gaussian Process (Constable and Parker, 1988) that follows Model G of McElhinny and McFadden (1997), which attributes the observed latitudinal dependence in directional dispersion to independent contributions from spherical harmonic families of odd and even symmetry for dynamo sources (**Section S1**). Modern studies of dispersion of paleomagnetic directions observed in lava flows from different areas as reliable instantaneous recorders of the geomagnetic field confirm that the ASD of the calculated VGPs roughly doubles from nominally 12° at the equator (K~46) to around 24° (K~11) by 60° and higher north and south latitudes (Cromwell et al., 2018; Johnson et al., 2008), as modeled by TK03 for a time-averaged GAD field.

Mean *Rc* can be calculated from individual inclinations converted with dipole formula to virtual geomagnetic latitudes in 5000 realizations of TK03 at every 5° of site latitude (**Table S1**). The resulting magnetic scaling factors are comparable to those for the other field models at geographic latitudes less than 30°; however, the TK03 scaling factors are appreciably lower at higher geographic latitudes, for example, 0.866 compared to 0.933 at 45° for the singular GAD model (**Fig. 5B**). Since the geocentric dipole typically represents more than 90% of the strength of the geomagnetic field at Earth's surface, much of this departure from the singular GAD model can be attributed to greater dipole wobble modeled by VGP poles with a more dispersed Fisherian distribution than SHA, for example, with about a nominal ASD=16° (K=27) (**Table S1**). Contributions from the much smaller nondipole field components, which TK03 fully represents (to degree and order 8) statistically by design, account for the yet larger departures of *f(Rc)* values because of averaging over a broader window of virtual geomagnetic latitudes. Parenthetically, we note that the magnitude of the key axial-dipole (g^0_1) term in TK03 has no impact on the VGP scatter produced by the statistical model (Cromwell et al., 2018) although a varying dipole moment is an important element of cosmic ray modulation.

2.4 Varying geomagnetic and heliomagnetic fields

Temporal variation in strength of the geomagnetic field expressed as M_t/M_0, the ratio of the average dipole moment from a given time (M_t) to its present-day value (M_0, ~ 80 ZAm^2), is the lead term in calculating *Rc* at any given site latitude (e.g., Equation 2 of Lifton et al., 2014) **(Fig. 6)**. Continuous empirical models for the axial dipole moment (ADM) such as GGF100k (Panovska et al., 2019), which we have chosen to use here (data listings available in the Earth Ref Digital Archive at https://earthref.org/ERDA/2382/), show that the dominant feature since 100 cal. ka is a distinct low associated with the Laschamp geomagnetic excursion at around 42 cal. ka (**Fig. 7A**). A cumulative plot of ADM as a proxy for the integrated shielding effect of a fluctuating dipole moment on ^{10}Be production shows that the time-averaged dipole moment has been within a few percent of a constant present-day fiducial back to around 20 cal. ka, which happens to encompass the age range of the primary ^{10}Be calibration sites (see below). The near-constant time-integrated dipole moment also renders schemes St and Lm as equivalent over this time frame. The ADM cumulative curve then gradually decreases to about 0.85 of a constant present-day fiducial from 20 cal. ka to around 50 cal. ka across the Laschamp excursion (**Fig. 7B**). We note that the time-varying ADM model also provides a broad framework for understanding well-calibrated production rate variations of cosmogenic ^{14}C in the atmosphere such as derived by (Fairbanks et al., 2005) where the long-term pattern of systematic age offsets, in this case calibrated by precise U-series dating on corals, can be linked to lower overall geomagnetic shielding of cosmic ray flux from lingering effects of the Laschamp excursion in conjunction with radiocarbon capture in short-term carbon cycling (**Fig. 7C**).

Solar modulation (*S*) of the interplanetary magnetic field generated by the Sun can variably deflect portions of the galactic cosmic ray flux impinging Earth (Gosse and Phillips, 2001; Lifton et al., 2005; Steinhilber et al., 2012). The solar magnetic field is closely associated with sunspot cycles where a higher solar magnetic field (and greater shielding of Earth's neighborhood in the solar system from galactic cosmic rays) occurs when sunspot numbers are higher, and *vice versa*. The 11-year sunspot (Schwabe) cycle is modulated by longer-period variations, such as the Gleissberg and Dalton minima and famously the first-named Maunder Grand Minimum, when sunspots were largely absent for practically a century. Such long solar magnetic minima should be times of relatively higher cosmic ray flux impinging Earth and are expected to be reflected in higher cosmogenic isotope production. This is indeed what has been reported using a variety of independently dated ice core and tree ring archives of cosmogenic nuclides (^{10}Be and ^{14}C) for the past 9.4 cal ka (Steinhilber et al., 2012) data available at https://www.ncei.noaa.gov/pub/data/paleo/climate_forcing/solar_variability/steinhilber2012.txt). The younger part of the record (**Fig. 8**) allows direct linkages of cosmogenic production rates to sunspot activity; the inferred relationship between solar magnetic field variations and cosmic ray intensity is extended to the rest of the available record back to 9.4 cal. ka based on the measured cosmogenic isotope production rates in the ice core and tree-ring archives.

Compared to the average cosmic ray intensity for 1944-1988 CE corresponding to relatively lively sunspot activity, most of the earlier part of the record has reduced sunspot activity that allowed higher cosmic ray flux to Earth. For example, cosmic ray flux for the Gleissberg, Dalton and Wolf grand solar minima was ~1.5 times higher and the Maunder and

Spörer grand solar minima more than 1.6 times higher than modern levels. A scaling factor, S_t/S_0, based on this record is incorporated in our R-routines (**Section S1**) in which relative ^{10}Be production at a given site varies directly with incremental cosmic ray intensity as estimated for the past 9.4 cal. ka, over which the flux (S_t/S_0) is on average a factor of 1.23 larger. In comparison, a weighted mean solar factor for the past 11.4 cal. ka based on the tree-ring radiocarbon record and used in scaling scheme Li (Balco et al., 2008) is only 1.05 (Lifton et al., 2005) although solar factors ~30% higher were predicted by (Desilets and Zreda, 2001). The same solar modulation framework of (Lifton et al., 2005) as implemented by (Balco et al., 2008) was later adopted in the LSD model by (Lifton et al., 2014), who explicitly chose not to explore alternative frameworks citing Steinhilber et al. (2008). More recent exchanges (e.g., Beer et al., 2018; Cameron and Schüssler, 2019; Usoskin et al., 2011) also indicate that further work is needed to determine how changes in the heliomagnetic field affect cosmic ray deflection.

3. Comparison of scaling schemes with primary ^{10}Be calibration sites

With these analytical tools in hand, we apply the different scaling schemes to the CRONUS-Earth primary ^{10}Be calibration sites (Borchers et al., 2016), as lodged in the ICE-D production rate online database (Martin et al., 2017) (**Section S2**). The ^{10}Be data were collected by modern sampling, laboratory and measurement protocols (e.g., referenced to 07KNSTD); local shielding and erosion corrections, typically a few percent, are accepted as given. Data relevant to determination of ^{10}Be production at each calibration locality with various scaling schemes are summarized in **Table 1**.

For MR (Macaulay Ridge, New Zealand), ^{10}Be concentrations are reported to average 89900 at/g for 7 boulder samples after taking into account corrections of 1-2% for sample thickness and local shielding, with a tight age constraint from ^{14}C AMS determinations of 9634±50 cal. years ago on wood fragments immediately beneath the rock slide (Putnam et al., 2010). Our implementation of the St scheme delivers a SLHL ^{10}Be production rate of 4.00 at/g/y for spallation with a ~2% contribution from muon processes (Balco, 2017), which when discounted gives 3.92 at/g/y that is reassuringly close to the rate of 3.84±0.08 at/g/y determined in more thorough online fashion for the St scheme by Putnam et al. (2010). When the ^{10}Be concentration is scaled according to *Rc* for a constant GAD or the comparable average ADM field and divided by the calibration age, a P_{SLHL} of about 4.16 at/g/y is obtained, which when discounted for ~2% muon contributions (4.1 at/g/y) is within the range of SLHL ^{10}Be production rates (3.74–4.15 at/g/y) quoted by the authors from the five scaling methods in online calculator v2 (Putnam et al., 2010). Scaling schemes that include secular variation of directions give higher total SLHL ^{10}Be production rates, 4.35 at/g/y for SHA and 4.52 at/g/y for TK03. The calibration age of MR is close to the older age limit of 9.4 cal. ka of the relative cosmic ray intensity record determined by Steinhilber et al. (2012), which would indicate that the SLHL ^{10}Be production rates determined by any of the scaling schemes should be increased by a factor of 1.23. This would imply that the estimated bracketing P_{SLHL} values for the St and TK03 scalings would range from 4.93 to 5.56 at/g/y (4.8 to 5.5 at/g/y for spallation only).

Comparable results are obtained from the primary calibration dataset for PPT (Promontory Point Terrace, Utah), providing P_{SLHL} bracketing total rates of 4.04 and 4.48 at/g/y for St and TK03 even though the calibration age (18.3 cal. ka) is almost twice as old as the one for MR (**Table 1**). Although the older calibration age for PPT makes it less clear how to factor in the higher relative cosmic ray intensity determined thus far for only the past 9.4 cal. ka (Steinhilber et al., 2012); a simple extension of the factor of 1.23 would imply that the estimated bracketing P_{SLHL} values for the St and TK03 scalings would range from 4.97 to 5.51 at/g/y (4.9 to 5.4 at/g/y for spallation only). Results reported for the SCOT (Scotland, United Kingdom) dataset provide similar P_{SLHL} bracketing total rates of 4.22 and 4.58 at/g/y for St and TK03, respectively; an extrapolation of the factor of 1.23 to the 11.7 cal. ka calibration age would imply that the estimated bracketing P_{SLHL} values for St and TK03 scalings would range from 5.20 to 5.63 at/g/y (5.1 to 5.5 at/g/y for spallation only).

The MR, PPT and SCOT data sets provide SLHL ^{10}Be production rates within about 5% of each other for any particular scaling scheme. Much more problematic is the primary calibration dataset HU08 based on glacial boulders from the high altitude (4859±9 m) and low latitude (13.9° S) Huancane site in Peru with a calibration age of 12.3 cal. ka. Samples from 10 glacial boulders give average P_{SLHL} ranging from 3.73 at/g/y for St to only 2.99 at/g/y for TK03, opposite to the low to high sense for these scaling schemes and as little as 60% of the more mutually consistent P_{SLHL} determined for MR, PPT and/or SCOT. The wide divergence of the Huancane P_{SLHL} may point to analytical shortcomings at the extreme of altitude ranges (Phillips et al., 2016b) (e.g., **Fig. 5A**). Contributing factors may be uncompensated effects of boulder surface erosion and weathering evidenced by 5-6 cm-high remnant pedestals (Kelly et al., 2015) and degraded sample bulk densities of only 2.29 g/cm^3 (Phillips et al., 2016a) compared to more typical bulk sample densities of around 2.7 g/cm^3 reported for the other calibration sites.

4. Significance for ^{10}Be exposure age at Allamuchy

Measured ^{10}Be concentrations for 13 boulders and glaciated surfaces at Allamuchy average 122000 at/g (Corbett et al., 2017) (**Table 1)**. Using SCOT calibrations, for example, P_{SLHL} values according to the various scaling schemes without the solar-factor would give exposure ages ranging from 22.7 to 24.2 cal. ka (22.3 to 23.8 cal. ka discounted 2% for muon contribution) for St and TK03, respectively, within but at the younger end of the age range of 25.2 ± 2.1 cal. ka reported with one standard deviation by Corbett et al. (2017) using the official CRONUS ^{10}Be production rates and array of scaling schemes. Similar exposure ages would be obtained for the MR and PPT calibrations, whose P_{SLHL} are about the same as for SCOT. However, using the anomalously low P_{SLHL} values determined from the HU08 calibration site would imply implausibly old exposure ages at Allamuchy, for example, 36.4 cal. ka using the P_{SLHL} rate of 3.0 at/g/y with TK03 even when discounted 2% for muon contribution.

Extending the average solar-factor determined for the past 9.4 years (Steinhilber et al., 2012) effectively decreases the calculated exposure ages for Allamuchy by 3/4 across all calibration schemes to be less than 20 cal. ka. For example, the resulting exposure ages (discounted for 2% muon production) for SCOT would be 18.1 cal. ka for St and 19.3 cal. ka for TK03. These age estimates that factor in the documented solar influence are much closer to the 16 cal. ka ^{14}C AMS dates on earliest terrestrial plant macrofossils in deglacial sediments on the Laurentide terminal moraine (Peteet et al., 2012).

5. Discussion

A plausible explanation for an exposure age of 25 cal. ka that we regard as anomalously old by some 9,000 years for LIS recession from its terminal moraine in northeastern North America is an undervalued solar modulation factor in estimates of the ^{10}Be production rate in the widely used online exposure age calculators from the published versions (v2, v2.2, v2.3; Balco et al., 2008) to the current online-only version (v3) of the 'online exposure age calculator formerly known as the CRONUS-Earth online exposure age calculator' (http://hess.ess.washington.edu/; https://cosmognosis.wordpress.com/2016/08/01/let-a-hundred-flowers-bloom/; last accessed 25May2023). A solar modulation factor for cosmic ray flux determined for the past 9.4 cal. ka

(Steinhilber et al., 2012) increases ^{10}Be production rates globally by an average of ~23%, which if applied to Allamuchy would reduce the previously calculated exposure age estimates of ~25 cal. ka (Corbett et al., 2017) to less than 20 cal. ka using any of the reliable (i.e., excluding HU08) ^{10}Be primary calibration data (**Table 1**). Additional localized factors could further decrease the likely ^{10}Be exposure ages for Allamuchy. For example, Corbett et al. (2017) pointed out that between-sample ^{10}Be concentrations for the erratic boulders and glaciated surfaces vary several times more than expected from analytical uncertainties alone, which could reflect the presence of inherited ^{10}Be in the sample population even though inheritance was ultimately discounted largely because of the widespread occurrence of glacial striations as indication of presumed sufficient abrasion of contaminating material from rock surfaces. Another contributing factor could stem from less shielding due to reduced atmospheric pressure during lowered sea level and/or from katabatic winds at the ice sheet margin in the early LIS recession stage (Staiger et al., 2007).

The inclusion of a solar modulation factor is expected to have broad ramifications to reported ^{10}Be exposure ages if it is indeed as large on average as the 23% determined for the past 9.4 cal. ka (Steinhilber et al., 2012). We believe such a percentage is already supported by bringing exposure ages at Allamuchy into reasonable alignment with reliable marine (sea-level, meltwater) and continental (earliest deglacial terrestrial plants) dating of Laurentide recession. As shown in **Table 1**, the St scheme as one of the three remaining favored schemes in v3 of the 'online exposure age calculator formerly known as the CRONUS-Earth online exposure age calculator' results in P(SLHL) for the MR, PPT and SCOT calibration sets of 4.0 to 4.2 at/g/y, in the neighborhood of what is currently regarded as the global value for ^{10}Be exposure dating (Borchers et al., 2016; Phillips et al., 2016a). However, adding the solar modulation factor would increase P(SLHL+S) to around 4.9 to 5.2 at/g/y and thus make ^{10}Be exposure dates proportionately younger. Scaling schemes that effectively include geomagnetic secular variation, such as the statistical TK03 model, have higher P(SLHL), which with solar modulation (according to Steinhilber et al., 2012) increase to around 5.5 at/g/y for spallation.

Adoption of ~4 at/g/y average P(SLHL) in CRONUS-Earth was partly due to including legacy scheme St, which runs notably low (~3 at/g/y) for the mid-latitude, low to moderate altitude calibration sites (MR, PPT and SCOT) compared to other scaling schemes (**Table 1**) yet P(SLHL) with scheme St for primary calibration site HU08 (3.73 at/g/y) is beguilingly close to those of the other calibration sites (4.00, 4.04 and 4.22 at/g/y for MR, PPT and SCOT, respectively). St assumes a static geomagnetic field with no secular variation and yet the magnetic scaling factor shows a more erratic pattern as a function of latitude than the schemes based on effective vertical cutoff rigidity (**Fig. 5B**). We suggest that an average P(SLHL+S) of 5.5±0.1 at/g/y based on the TK03 scaling scheme for MR, PPT and SCOT calibration sites that includes a solar modulation factor of 1.23 (and is discounted 2% for muon contribution) provides a good working estimate for exposure age determinations as far back as 20 cal. ka, beyond which a lower average geomagnetic dipole moment (that would tend to increase ^{10}Be production rates) needs to be taken into account. Compared to the currently accepted CRONUS consensus P(SLHL) of ~4.0 at/g/y, this would reduce exposure ages to nominally ~3/4 of the quoted values.

Another indication that the SLHL ^{10}Be reference production rate is appreciably higher than the currently used level of ~4 at/g/y comes from attempts to include glacial isostatic adjustment (GIA) in exposure dating. For example, Lowell et al. (2021) report ^{10}Be exposure dates using a SLHL ^{10}Be production rate of 4.3 at/g/y from Balco et al. (2009) on glacial boulders along a 375 km transect just west of Lake Superior (see **Fig. 1** for transect location) perpendicular to the retreating margin of the southwestern Labrador lobe of the LIS as delineated by radiocarbon isochrons (Dalton et al., 2020). According to the ^{10}Be exposure dates, deglaciation occurred by ~18 cal. ka near the projected southwestern end of the transect at Kylen Lake and by ~10.5 cal. ka near Pillar at the northeastern end at a mean retreat rate of ~50 km/kyr (thick red line in **Fig. 9**). Over the same transect, isochrons of ice-margin retreat derived from radiocarbon ages of deglacial deposits converted to calendar years in Lowell et al. (2021) are up to 4 ka *younger*. A related problem emerges with the stated inability to correct the ^{10}Be ages for changes in elevation due to uplift from GIA. Even updated GIA model ICE-6G (Peltier et al., 2015) produces adjusted ^{10}Be ages that are deemed to be unacceptably up to ~10% older, for example, increasing the ^{10}Be age from 17.4 to 19.2 cal. ka for sample AF-109 and 15.3 to 16.4 cal. ka for sample AF-110 near the southern end of the transect (Supplemental Material text 1.3 and Table S4 in Lowell et al., 2021). However, if a SLHL ^{10}Be production rate of ~5.3 at/g/y that included a solar modulation factor of 1.23 was used, the ^{10}Be date for sample AF-109 would be only 15.3 cal. ka (and sample AF-110 would be 13.4 cal. ka) after uplift correction with GIA model ICE-6G as implemented in the iceTEA online toolkit (Jones et al., 2019). The average retreat rate would be faster (~70 km/kyr, dashed line in **Fig. 9**) and the recession trajectory would be mostly within the radiocarbon isochron error envelope.

The stated anchor of the transect to the southwest was a basal radiocarbon age of 18.1 cal. ka from sediment cores at Kylen Lake. However, Lund and Banerjee (1985) reported a major age reversal of several thousand years in bulk sediment radiocarbon ages at the base of one of the Kylen Lake cores with palynological evidence for the classic landscape ragweed disturbance (*Ambrosia*) up-core almost 1 cal. ka off, and warned that the radiocarbon dates were likely contaminated and too old. The problem was acknowledged by Lowell et al. (2021) but following an evaluation of radiocarbon dates from prior work as well as radiocarbon dates from a new sediment core from Kylen Lake in an unpublished thesis (Norris, 2019), a modeled basal age of 18.1 cal. ka from Kylen Lake was nevertheless used to anchor the transect in the shifting shoals of bulk sediment radiocarbon dating.

A more recent example of potential implications of recognizing significant solar modulation of cosmic ray flux is in a study of cosmogenic-nuclide concentrations in subglacial bedrock cores between Thwaites and Pope glaciers in Antarctic where Balco et al. (2023) argued that the West Antarctic Ice Sheet (WAIS) at the site was about 35 m thinner several thousand years ago and subsequently thickened to its present thickness. The conclusion basically followed from modeling the concentrations of ^{10}Be, ^{26}Al and ^{14}C measured in cores of the subglacial bedrock that were higher than expected from shielding by present ice thickness, implicitly assuming a uniform present-day cosmic ray flux over the entire Holocene. However, Steinhilber et al. (2012) showed that the average cosmic ray flux was about 50% higher about 7.5 cal. ka and decreased to modern levels by around 2.5 cal. ka before increasing to another series of peaks during the Spörer and Maunder solar minima in the last millennium before decreasing to present-day levels (**Fig. 8B**). This suggests an alternative interpretation of the variable cosmogenic-nuclide concentrations whereby the ice thickness for WAIS at that locale may have stayed approximately the same for the past ~6 cal. ka but a varying cosmic ray flux caused commensurate changes in the cosmogenic-nuclide production rate and hence accounted for much of the observed age-dependent pattern of their subglacial bedrock concentrations.

Other implications of a significant solar modulation factor exist but are less immediately obvious considering the wide range of SLHL ^{10}Be production rates from around 6 to 4 at/g/y that have been used in more than 30 years of published investigations. Normalization of these results to a consistent SLHL ^{10}Be production rate and scaling scheme would be revealing.

6. Conclusions

• The anomalously old ^{10}Be exposure dates for LIS recession in northeastern North America of ~25 cal. ka, such as at Allamuchy, which are inconsistent with independently documented timing of meltwater production and global sea level rise from the marine record and are not supported by ^{14}C AMS dates on terrestrial plant macrofossils in early deglacial sediments, point to a deficiency in the ^{10}Be exposure dating methodology.

• The incorporation of a published but apparently unutilized solar modulation factor results in an average increase by about a factor of 1.23 in cosmic ray intensity compared to the modern over the 9.4 cal. ka length of the currently available record. This decreases ^{10}Be exposure ages to about ¾ of stated values and in the case of Allamuchy to less than 20 cal. ka, which works toward resolving the glaring age discrepancy with the marine record and reliable radiocarbon dates in the terrestrial realm.

• Secular variation in geomagnetic field directions could be conveniently represented in scaling schemes on time scales of several millennia and longer using a globally valid statistical field model (TK03) that incorporates secular variation with non-dipole components and results in SLHL ^{10}Be production rates for mid-latitude sites that are about 10% higher than with conventional models that have little (e.g., SHA.DIF.14k) to no (geocentric axial dipole or GAD) directional disperson.

• Estimates of the axial dipole moment such as GGF100k have a time-integrated mean at about the present-day field value going back to ~20 cal. ka, decreasing to about 0.85 of the modern value only by ~50 cal. ka. Geomagnetic field strength thus does not appear to be a critical factor in exposure dating over the latest Pleistocene and Holocene.

• An average P(SLHL+S) of 5.5 at/g/y based on extending the published solar modulation factor of 1.23 for the past 9.4 cal. ka and using the TK03 magnetic scaling scheme for mid latitude calibration sites produces a reasonable fit to GIA model ICE-6G of exposure age data from the Labrador Dome of the LIS along a transect just west of Lake Superior.

• Changes in observed ^{10}Be production in subglacial bedrock due to known variable solar modulation provides an alternative explanation to changes in shielding from variation in thickness of West Antarctic ice sheet, providing another line of evidence to test implications of large-amplitude solar modulation.

Author contributions

Authorship in alphabetical order. DP initiated the study and assessed radiocarbon dates, LL wrote the R-code and incorporated solar modulation influences, DK incorporated geomagnetic field models and prepared the draft of the manuscript with DP and LL.

Competing interests

The authors declare that they have no conflict of interest.

Acknowledgements

Our collaborative effort sprang from a presentation on the subject by DP at a Memorial Symposium for Wally Broecker in 2019 and eventually came to fruition after Covid shutdowns. We appreciate the detailed critical comments by two anonymous reviewers on an earlier version of the manuscript, which helped us to focus on the scaling schemes and solar modulation. Work was supported by NASA (DP), the University of Urbino (LL), and the Lamont Paleomagnetic Research Fund (DK).

References

Aab, A., and others, 2017. The Pierre Auger Collaboration. Science 357, 1266, 1210.1126/science.aan4338.

Balco, G., 2017. Production rate calculations for cosmic-ray-muon-produced 10Be and 26Al benchmarked against geological calibration data. Quaternary Geochronology 39, 150-173.

Balco, G., Briner, J., Finkel, R.C., Rayburn, J.A., Ridge, J.C., Schaefer, J.M., 2009. Regional beryllium-10 production rate calibration for late-glacial northeastern North America. Quaternary Geochronology 4, 93-107.

Balco, G., Brown, N., Nichols, K., Venturelli, R.A., Adams, J., Braddock, S., Campbell, S., Goehring, B., Johnson, J.S., Rood, D.H., Wilcken, K., Hall, B., Woodward, J., 2023. Reversible ice sheet thinning in the Amundsen Sea Embayment during the Late Holocene. The Cryosphere 17, 1787-1801.

Balco, G., Schaefer, J.M., 2006. Cosmogenic-nuclide and varve chronologies for the deglaciation of southern New England Quaternary Geochronology 1, 15-28.

Balco, G., Stone, J.O., Lifton, N.A., Dunai, T.J., 2008. A complete and easily accessible means of calculating surface exposure ages or erosion rates from 10Be and 26Al measurements. Quaternary Geochronology 3, 174–195.

Balco, G., Stone, J.O.H., Porter, S.C., Caffee, M.W., 2002. Cosmogenic-nuclide ages for New England coastal moraines, Martha’s Vineyard and Cape Cod, Massachusetts, USA. Quaternary Science Reviews 21, 2127–2135.

Beer, J., Tobias, S.M., Weiss, N.O., 2018. On long-term modulation of the Sun's magnetic cycle. Monthly Notices of the Royal Astronomical Society 473, 1596-1602.
Birks, H., 1993. The importance of plant macrofossils in late-glacial climatic reconstructions : an example from western Norway. Quaternary Science Reviews 12, 719-726.
Birks, H.H., 2002. Plant macrofossils, in: Smol, J.P., Birks, H.J.B., Last, W.M. (Eds.), Tracking Environmental Change Using Lake Sediments, vol Kluwer Academic Publishers, Dordrecht, pp. 49–74.
Borchers, B., Marrero, S., Balco, G., Caffee, M., Goehring, B., Lifton, N., Nishiizumi, K., Phillips, F., Schaefer, J., Stone, J., 2016. Geological calibration of spallation production rates in the CRONUS-Earth project. Quaternary Geochronology 31, 188-198.
Cameron, R.H., Schüssler, M., 2019. Solar activity: periodicities beyond 11 years are consistent with random forcing. A&A 625, A28.
Chapin, F.S., Walker, L.R., Fastie, C.L., Sharman, L.C., 1994. Mechanisms of Primary Succession Following Deglaciation at Glacier Bay, Alaska. Ecological Monographs 64, 149-175.
Clark, P.U., Mix, A.C., 2002. Ice sheets and sea level of the Last Glacial Maximum. Quaternary Science Reviews 21, 1-7.
Constable, C.G., Parker, R.L., 1988. Statistics of the geomagnetic secular variation for the past 5 m.y. Journal of Geophysical Research 93, 11,569-511,581.
Cooper, W.S., 1923. The recent ecological history of Glacier Bay, Alaska. II. The present vegetation cycle. Ecology 4, 223- 246.
Corbett, L.B., Bierman, P.R., Stone, B.D., Caffee, M.W., Larsen, P.L., 2017. Cosmogenic nuclide age estimate for Laurentide Ice Sheet recession from the terminal moraine, New Jersey, USA, and constraints on latest Pleistocene ice sheet history. Quaternary Research 87, 482-498.
Cotter, J.F.P., 1983. The Minimum age of the Woodfordian Deglaciation of Northeastern Pennsylvania and Northwestern New Jersey. Lehigh University, Bethlehem, p. 159.
Cromwell, G., Johnson, C.L., Tauxe, L., Constable, C.G., Jarboe, N.A., 2018. PSV10: A Global Data Set for 0–10 Ma Time-Averaged Field and Paleosecular Variation Studies. Geochemistry, Geophysics, Geosystems 19, 1533-1558.
Curry, B., Konen, M., Larson, T., Yansa, C., Hackley, K., Alexanderson, H., Lowell, T., 2010. The DeKalb mounds of northeastern Illinois as archives of deglacial history and postglacial environments. Quaternary Research 74, 82–90, doi:10.1016/j.yqres.2010.1004.1009.
Dalton, A.S. and others, 2020. An updated radiocarbon-based ice margin chronology for the last deglaciation of the North American Ice Sheet Complex. Quaternary Science Reviews 234, 106223.
Desilets, D., Zreda, M., 2001. On scaling cosmogenic nuclide production rates for altitude and latitude using cosmic-ray measurements. Earth and Planetary Science Letters 193, 213-225.
Desilets, D., Zreda, M., Lifton, N.A., 2001. Comment on 'Scaling factors for production rates of in situ produced cosmogenic nuclides: a critical reevaluation' by Tibor J. Dunai. Earth and Planetary Science Letters 188, 283-287.
Desilets, D., Zreda, M., Prabu, T., 2006. Extended scaling factors for in situ cosmogenic nuclides: New measurements at low latitude. Earth and Planetary Science Letters 246, 265–276.
Dunai, T.J., 2000. Scaling factors for production rates of in situ produced cosmogenic nuclides: a critical reevaluation. Earth and Planetary Science Letters 176, 157^169.
Dunai, T.J., 2001. Reply to comment on 'Scaling factors for production rates of in situ produced cosmogenic nuclides: a critical reevaluation' by Darin Desilets, Marek Zreda and Nathaniel Lifton. Earth and Planetary Science Letters 188, 289-298.
Dyke, A.S., Moore, A., Robertson, L., 2003. Deglaciation of North America. Geological Survey of Canada Open File 1574.
Elsasser, W., E. P. Ney, Winckler, J.R., 1956. Cosmic-ray intensity and geomagnetism. Nature 178, 1226–1227.
Fairbanks, R.G., Mortlock, R.A., Chiu, T.-C., Cao, L., Kaplan, A., Guilderson, T.P., Fairbanks, T.W., Bloom, A.L., Grootes, P.M., Nadeau, M.-J., 2005. Radiocarbon calibration curve spanning 0 to 50,000 years BP based on paired 230Th/234U/238U and 14C dates on pristine corals. Quaternary Science Reviews 24, 1781-1796.

Fickert, T., Friend, D., Grüninger, F., Molnia, B., Richter, M., 2007. Did Debris-Covered Glaciers Serve as Pleistocene Refugia for Plants? A New Hypothesis Derived from Observations of Recent Plant Growth on Glacier Surfaces. Arctic, Antarctic, and Alpine Research 39, 245-257.
Flower, B.P., Hastings, D.W., Hill, H.W., Quinn, T.M., 2004. Phasing of deglacial warming and Laurentide Ice Sheet meltwater in the Gulf of Mexico. Geology 32, 597-600.
Gaglioti, B.V., Mann, D.H., Jones, B.M., Pohlman, J.W., Kunz, M.L., Wooller, M.J., 2014. Radiocarbon age-offsets in an arctic lake reveal the long-term response of permafrost carbon to climate change. Journal of Geophysical Research: Biogeosciences 119, 1630-1651.
Gosse, J.C., Phillips, F.M., 2001. Terrestrial in situ cosmogenic nuclides: theory and application. Quaternary Science Reviews 20, 1475-1560.
Grimm, E.C., Maher, L.J., Nelson, D.M., 2009. The magnitude of error in conventional bulk-sediment radiocarbon dates from central North America. Quaternary Research 72, 301-308.
Hajdas, I., Ivy, S.D., Beer, J., Bonani, G., Imboden, D., Lotter, A.F., Sturm, M., Suter, M., 1993. AMS radiocarbon dating and varve chronology of Lake Soppensee e 6000 to 12000 14C years BP. Climate Dynamics 9, 107e116.
Harmon, K., 1968. Late Pleistocene Forest Succession in Northern New Jersey. Rutgers University, New Brunswick, NJ.
Johnson, C.L., Constable, C.G., Tauxe, L., Barendregt, R., Brown, L.L., Coe, R.S., Layer, P., Mejia, V., Opdyke, N.D., Singer, B.S., Staudigel, H., Stone, D.B., 2008. Recent investigations of the 0–5 Ma geomagnetic field recorded by lava flows. Geochemistry Geophysics Geosystems 9, Q04032, doi:04010.01029/02007GC001696
Jones, G.A., Henry, G.H.R., 2003. Primary plant succession on recently deglaciated terrain in the Canadian High Arctic. Journal of Biogeography 30, 277–296.
Jones, R.S., Small, D., Cahill, N., Bentley, M.J., Whitehouse, P.L., 2019. iceTEA: Tools for plotting and analysing cosmogenic-nuclide surface-exposure data from former ice margins. Quaternary Geochronology 51, 72-86.
Karrow, P.F., Warner, B.G., Fritz, P., 1986. Reply to J. F. P. Cotter, E. B. Evenson, L. Sirkin, and R. Stuckenrath,. Quaternary Research 25, 259–262, doi:210.1016/0033-5894(1086)90063-90063.
Keigwin, L.D., Jones, G.A., Lehman, S.J., Boyle, E.A., 1991. Deglacial meltwater discharge, North Atlantic Deep Circulation, and abrupt climate change. Journal of Geophysical Research: Oceans 96, 16811-16826.
Kelly, M.A., Lowell, T.V., Applegate, P.J., Phillips, F.M., Schaefer, J.M., Smith, C.A., Kim, H., Leonard, K.C., Hudson, A.M., 2015. A locally calibrated, late glacial 10Be production rate from a low-latitude, high-altitude site in the Peruvian Andes. Quaternary Geochronology 26, 70-85.
Lal, D., 1991. Cosmic ray labeling of erosion surfaces: in situ nuclide production rates and erosion models. Earth and Planetary Science Letters 104, 424-439.
Lambeck, K., Rouby, H., Purcell, A., Sun, Y., Sambridge, M., 2014. Sea level and global ice volumes from the Last Glacial Maximum to the Holocene. Proceedings of the National Academy of Sciences 111, 15296.
Larsen, P., 1996. In-situ production rates of cosmogenic 10Be and 26Al over the past 21,500 years determined from the terminal moraine of the Laurentide Ice Sheet, north-central New Jersey. University of Vermont, Burlington, p. 128.
Lifton, N., Sato, T., Dunai, T.J., 2014. Scaling in situ cosmogenic nuclide production rates using analytical approximations to atmospheric cosmic-ray fluxes. Earth and Planetary Science Letters 386, 149-160.
Lifton, N.A., Bieber, J.W., Clem, J.M., Duldig, M.L., Evenson, P., Humble, J.E., Pyle, R., 2005. Addressing solar modulation and long-term uncertainties in scaling secondary cosmic rays for in situ cosmogenic nuclide applications. Earth and Planetary Science Letters 239, 140-161.
Lowell, T.V., Kelly, M.A., Howley, J.A., Fisher, T.G., Barnett, P.J., Schwart, R., Zimmerman, S.R.H., Norris, N., Malone, A.G.O., 2021. Near-constant retreat rate of a terrestrial margin of the Laurentide Ice Sheet during the last deglaciation. Geology 49, 1511-1515.
Lund, S.P., Banerjee, S.K., 1985. Late Quaternary paleomagnetic field secular variation from two Minnesota lakes. Journal of Geophysical Research 90, 803-825.
MacDonald, G.M., Beukens, R.P., Kieser, W.E., Vitt, D.H., 1987. Comparative radiocarbon dating of terrestrial plant macrofossils and aquatic moss from the "ice-free corridor" of western Canada. Geology 15, 837–840.

Marrero, S.M., Phillips, F.M., Borchers, B., Lifton, N., Aumer, R., Balco, G., 2016. Cosmogenic nuclide systematics and the CRONUScalc program. Quaternary Geochronology 31, 160-187.

Martin, L.C.P., Blard, P.H., Balco, G., Lavé, J., Delunel, R., Lifton, N., Laurent, V., 2017. The CREp program and the ICE-D production rate calibration database: A fully parameterizable and updated online tool to compute cosmic-ray exposure ages. Quaternary Geochronology 38, 25-49.

Marty, J., Myrbo, A., 2014. Radiocarbon dating suitability of aquatic plant macrofossils. Journal of Paleolimnology 52, 435-443.

Matthews, J.A., 1992. The ecology of recently-deglaciated terrain : a geoecological approach to glacier forelands and primary succession. University Press, Cambridge, New York.

McElhinny, M.W., McFadden, P.L., 1997. Paleosecular variation over the past 5 Myr based on a new generalized database. Geophysical Journal International 131, 240-252.

Norris, N., 2019. The Mystery Interval: hydrologic changes and circulation pattern changes? University of Cincinnati, p. 63.

Paillard, D., Labeyrie, L., Yiou, P., 1996. Macintosh program performs time-series analysis. Eos Transactions AGU 77, 379.

Panovska, S., Korte, M., Constable, C.G., 2019. One hundred thousand years of geomagnetic field evolution. Reviews of Geophysics 57, 1289-1337.

Pavón-Carrasco, F.J., Osete, M.L., Torta, J.M., De Santis, A., 2014. A geomagnetic field model for the Holocene based on archaeomagnetic and lava flow data. Earth and Planetary Science Letters 388, 98-109.

Peltier, W.R., Argus, D.F., Drummond, R., 2015. Space geodesy constrains ice age terminal deglaciation: The global ICE-6G_C (VM5a) model. Journal of Geophysical Research: Solid Earth 120, 450-487.

Peteet, D.M., Beh, M., Orr, C., Kurdyla, D., Nichols, J., Guilderson, T., 2012. Delayed deglaciation or extreme Arctic conditions 21-16 cal. kyr at southeastern Laurentide Ice Sheet margin? Geophysical Research Letters 39, L11706, doi:11710.11029/12012GL051884.

Peteet, D.M., Daniels, R.A., Heusser, L.E., Vogel, J.S., Southon, J.R., Nelson, D.E., 1993. Late-glacial pollen, macrofossils and fish remains in Northeastern, USA: The Younger Dryas oscillation. Quaternary Science Reviews 12, 597-612, doi:510.1016/0277-3791(1093)90002-90004.

Peteet, D.M., Mann, D.H., 1994. Late-glacial vegetational, tephra, and climatic history of southwestern Kodiak Island, Alaska. Ecoscience 1, 255-267.

Peteet, D.M., Vogel, J.S., Nelson, D.E., Southon, J.R., Nickmann, R.J., Heusser, L.E., 1990. Younger Dryas climatic reversal in northeastern USA? AMS ages for an old problem. Quaternary Research 33, 219-230, doi:210.1016/0033-5894(1090)90020-L.

Phillips, F.M., Argento, D.C., Balco, G., Caffee, M.W., Clem, J., Dunai, T.J., Finkel, R., Goehring, B., Gosse, J.C., Hudson, A.M., Jull, A.J.T., Kelly, M.A., Kurz, M., Lal, D., Lifton, N., Marrero, S.M., Nishiizumi, K., Reedy, R.C., Schaefer, J., Stone, J.O.H., Swanson, T., Zreda, M.G., 2016a. The CRONUS-Earth Project: A synthesis. Quaternary Geochronology 31, 119-154.

Phillips, F.M., Argento, D.C., Bourlès, D.L., Caffee, M.W., Dunai, T.J., Goehring, B., Gosse, J.C., Hudson, A.M., Jull, A.J.T., Kelly, M., Lifton, N., Marrero, S.M., Nishiizumi, K., Reedy, R.C., Stone, J.O.H., 2016b. Where now? Reflections on future directions for cosmogenic nuclide research from the CRONUS Projects. Quaternary Geochronology 31, 155-159.

Putnam, A.E., Schaefer, J.M., Barrell, D.J.A., Vandergoes, M., Denton, G.H., Kaplan, M.R., Finkel, R.C., Schwartz, R., Goehring, B.M., Kelley, S.E., 2010. In situ cosmogenic 10Be production-rate calibration from the Southern Alps, New Zealand. Quaternary Geochronology 5, 392-409.

R_Core_Team, 2018. R: A language and environment for statistical computing, available at http://www.r-project.org.

Sirkin, L., Stuckenrath, R., 1980. The Port Washingtonian warm interval in the northern Atlantic coastal plain. Geological Society of America Bulletin 91, 332–336.

Staiger, J., Gosse, J., Toracinta, R., Oglesby, B., Fastook, J., Johnson, J., 2007. Atmospheric scaling of cosmogenic nuclide production: climate effect. Journal of Geophysical Research 112, BO2205.

Stanford, S.D., Stone, B.D., Ridge, J.C., Witte, R.W., Pardi, R.R., Reimer, G.E., 2020. Chronology of Laurentide glaciation in New Jersey and the New York City area, United States. Quaternary Research 99, 142-167.

Steinhilber, F., Abreu, J.A., Beer, J., 2008. Solar modulation during the Holocene. Astrophys. Space Sci. Trans. 4, 1-6.
Steinhilber, F., Abreu, J.A., Beer, J., Brunner, I., Christl, M., Fischer, H., Heikkilä, U., Kubik, P.W., Mann, M., McCracken, K.G., Miller, H., Miyahara, H., Oerter, H., Wilhelms, F., 2012. 9,400 years of cosmic radiation and solar activity from ice cores and tree rings. Proceedings of the National Academy of Sciences 109, 5967.
Stone, J.O., 2000. Air pressure and cosmogenic isotope production. Journal of Geophysical Research: Solid Earth 105, 23753-23759.
Tarasov, L., Dyke, A.S., Neal, R.M., Peltier, W.R., 2012. A data-calibrated distribution of deglacial chronologies for the North American ice complex from glaciological modeling. Earth and Planetary Science Letters 315-316, 30-40.
Tauxe, L., Kent, D.V., 2004. A simplified statistical model for the geomagnetic field and the detection of shallow bias in paleomagnetic inclinations: Was the ancient magnetic field dipolar?, in: Channell, J.E.T., Kent, D.V., Lowrie, W., Meert, J. (Eds.), Timescales of the Paleomagnetic Field, Geophysical Monograph 145. American Geophysical Union, Washington, D.C., pp. 101–116.
Thompson, W.B., Dorion, C., Ridge, J.C., Balco, G., Fowler, B., Svendsen, K., 2017. Deglaciation and late-glacial climate change in the White Mountains, New Hampshire. Quaternary Research 87, 96-120.
Usoskin, I.G., Bazilevskaya, G.A., Kovaltsov, G.A., 2011. Solar modulation parameter for cosmic rays since 1936 reconstructed from ground-based neutron monitors and ionization chambers. Journal of Geophysical Research: Space Physics 116.
Wickert, A.D., Williams, C., Gregoire, L.J., Callaghan, K.L., Ivanović, R.F., Valdes, P.J., Vetter, L., Jennings, C.E., 2023. Marine-Calibrated Chronology of Southern Laurentide Ice Sheet Advance and Retreat: ~2,000-Year Cycles Paced by Meltwater–Climate Feedback. Geophysical Research Letters 50, e2022GL100391.
Zimmerman, S., Wahl, D., 2020. Holocene paleoclimate change in the western US: The importance of chronology in discerning patterns and drivers. Quaternary Science Reviews 246, 106487, doi:106410.101016/j.quascirev.102020.106487.

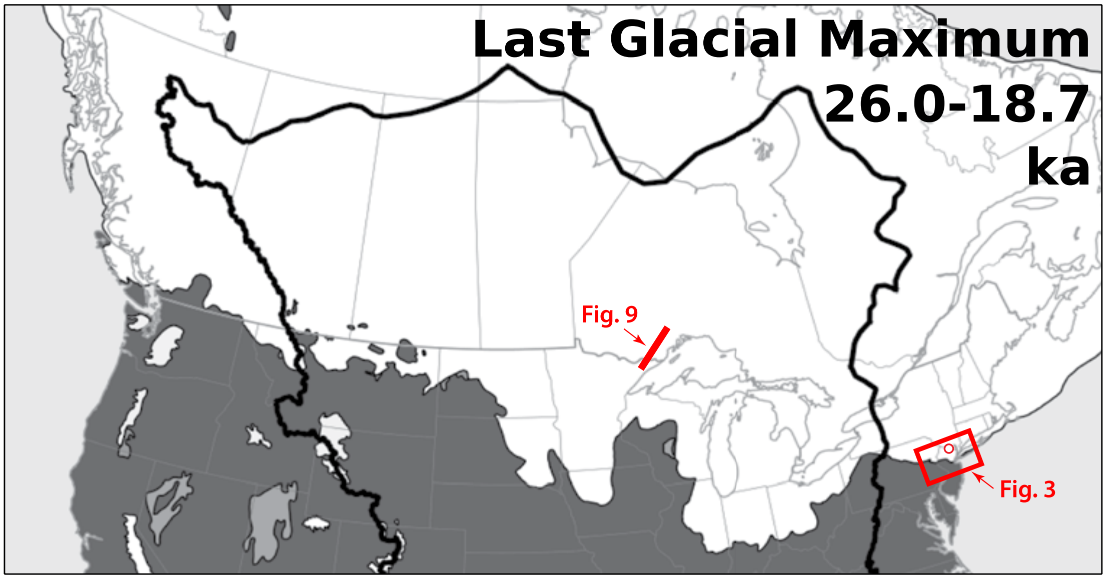

Fig. 1. Synthesis of southern Laurentide ice sheet (white area) during Last Glacial Maximum from 26.0 - 18.7 cal. ka (figure from Wickert et al., 2023) based on revised dates from Dalton et al. (2020) modified to fit a marine chronology. Lakes are medium gray, land is dark gray, and oceans are light gray; associated Mississippi River drainage-basin extent shown by heavy black line. Box shows location of map in **Fig. 3** and includes locale (small red open circle) of terminal moraine at Allamuchy and environs studied by Corbett et al. (2017); thick red line shows the approximate location of transect studied by Lowell et al. (2021) and shown in **Fig. 9**.

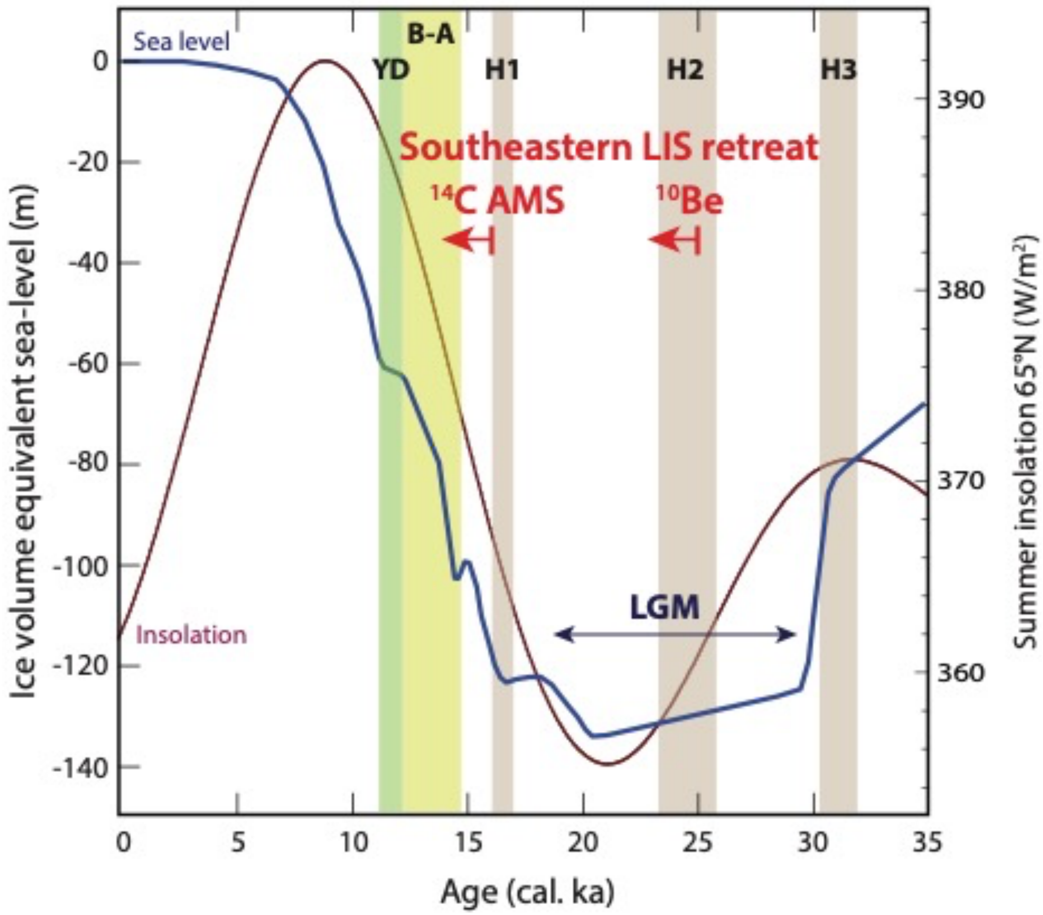

Fig. 2. Contrasting age estimates for deglaciation of southeastern lobe of Laurentide ice sheet (LIS) based on ^{14}C AMS dating of earliest terrestrial plant macrofossils in deglacial sediments (Peteet et al., 2012) and on ^{10}Be exposure dating for terminal moraine in Allamuchy area of New Jersey (Corbett et al., 2017), plotted with respect to major climate events (Last Glacial Maximum, (LGM), Heinrich events H1, H2 and H3, the Bolling-Allerod warm period (B-A) and the Younger Dryas cold period (YD), estimated ice-volume equivalent sea-level change (blue curve) since 35 cal. ka (from Lambeck et al., 2014), and summer insolation at 65°N (maroon curve, calculated with Paillard et al. (1996)). See Peteet et al. (2012) for additional climate proxies and discussion.

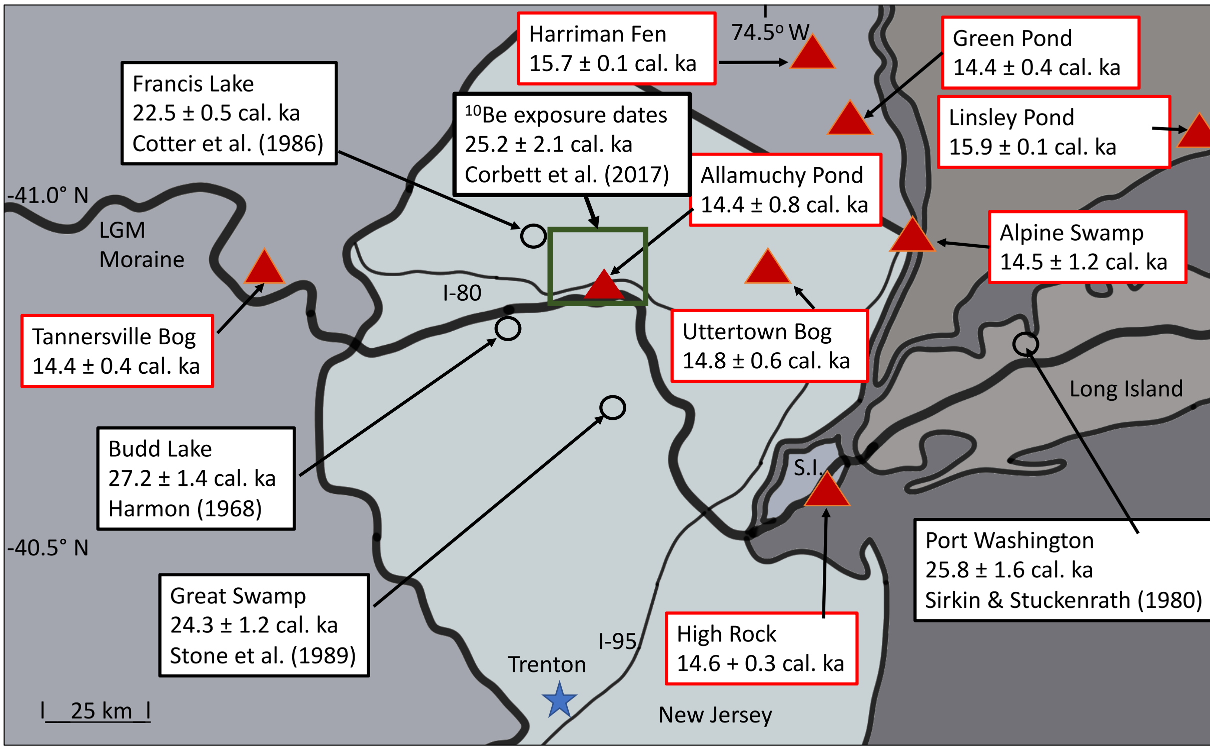

Fig. 3. ^{14}C AMS dates on plant macrofossils in earliest deglacial sediments (red triangles; Peteet et al., 2012), ^{14}C bulk sediment dates (open circles with references in labels), and ^{10}Be exposure dates from glacial boulders and pavement within the box around Allamuchy Pond that outlines study region in Fig. 2 of Corbett et al. (2017) associated with the retreat of the southeastern lobe of the LIS in northern NJ and southern NY. Figure adapted from Corbett et al. (2017).

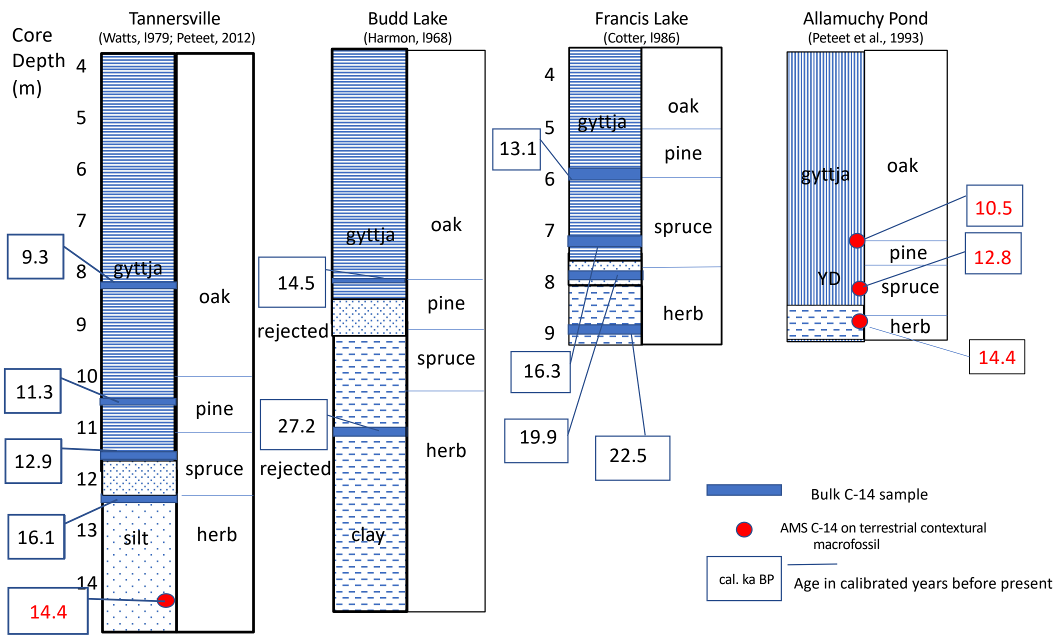

Fig. 4. Radiocarbon dates in context of litho- and bio-stratigraphy of cores from ponds and lakes in close proximity to terminal moraine of Laurentide ice sheet at LGM in northern NJ (see **Fig. 3** for locations). Bulk sediment ^{14}C dates from gytjja, silts, or clay (stratigraphic layers) are indicated in black; ^{14}C AMS dates on identified terrestrial macrofossils are indicated in red (from Peteet et al., 2012).

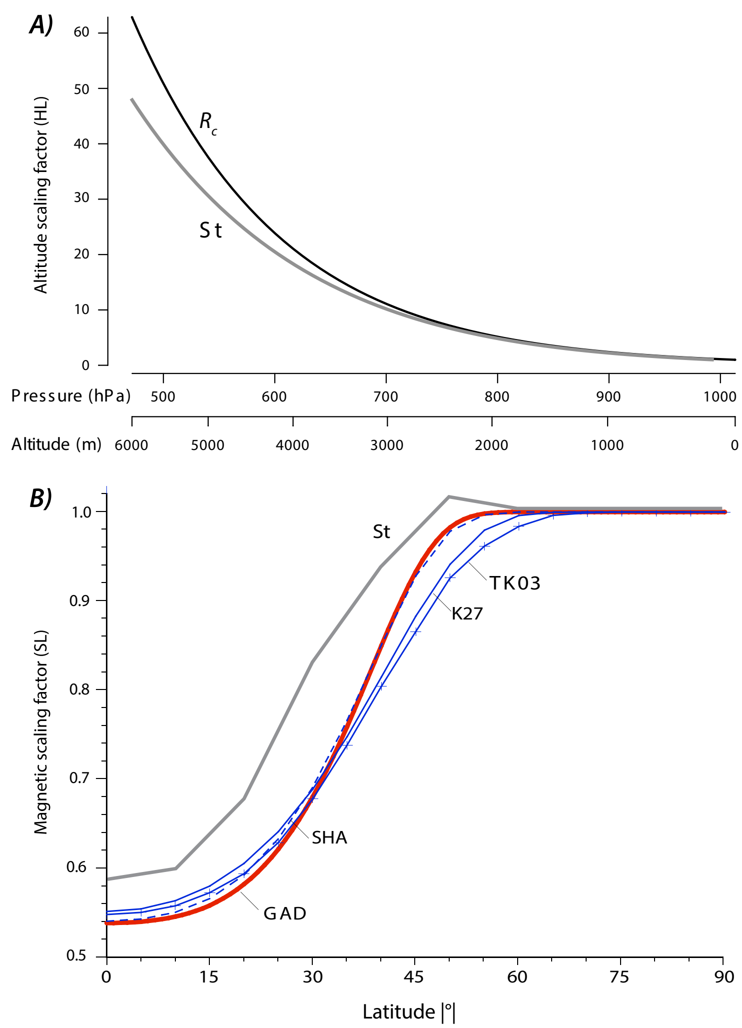

Fig. 5. Altitude and latitude scaling factors. A) Altitude scaling factor at high latitude (HL) versus air pressure and equivalent altitude for St, the Lal/Stone empirical scaling scheme (Stone, 2000) and the analytical scaling scheme based on effective vertical cutoff rigidity, R_c (Desilets et al., 2006; Lifton et al., 2014). B) Magnetic scaling factor for different schemes including empirical St (Stone, 2000) and those based on effective vertical cutoff rigidity, *Rc,* using Equation 2 of Lifton et al. (2014) to derive a magnetic scaling factor, *f(Rc)* (Desilets et al., 2006) with modern magnetic moment (~80 Am^2) as functions of latitude according to different geomagnetic field models: GAD, geomagnetic axial dipole field with no dispersion; K118 (SHA), mean VGP from SHA.DIF.14k model of Pavón-Carrasco et al. (2014) for 0-14 cal. ka with equivalent Fisher precision parameter K=118; K27, GAD field with Fisher distribution of VGP of K=27; TK03, statistical geomagnetic field model of Tauxe and Kent (2004).

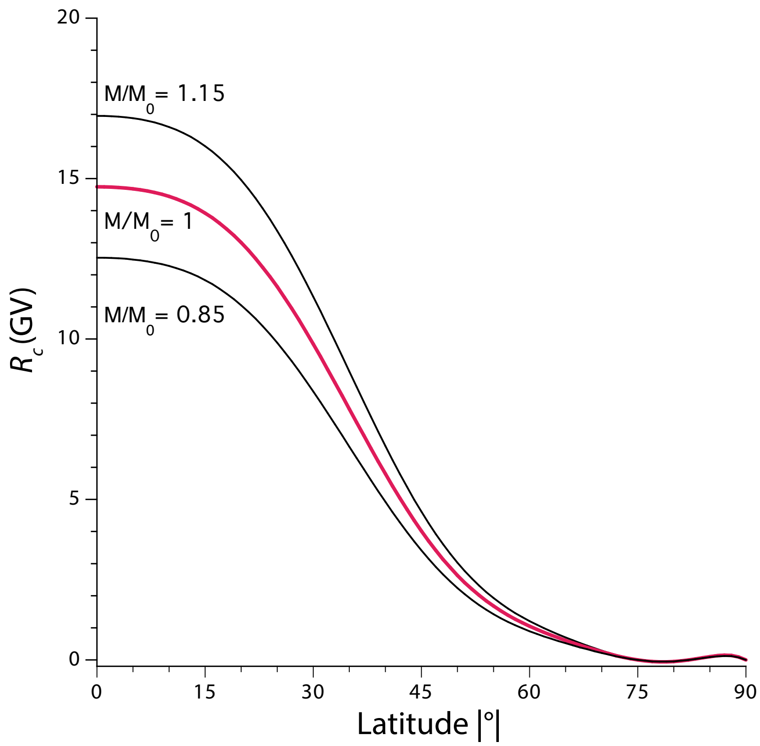

Fig. 6. Effective vertical cutoff rigidity (R_c) as a function of geomagnetic latitude for a representative range of dipole moments ($\boldsymbol{M}$) relative to the modern value ($\boldsymbol{M_0}$) calculated with Equation 2 of Lifton et al. (2014).

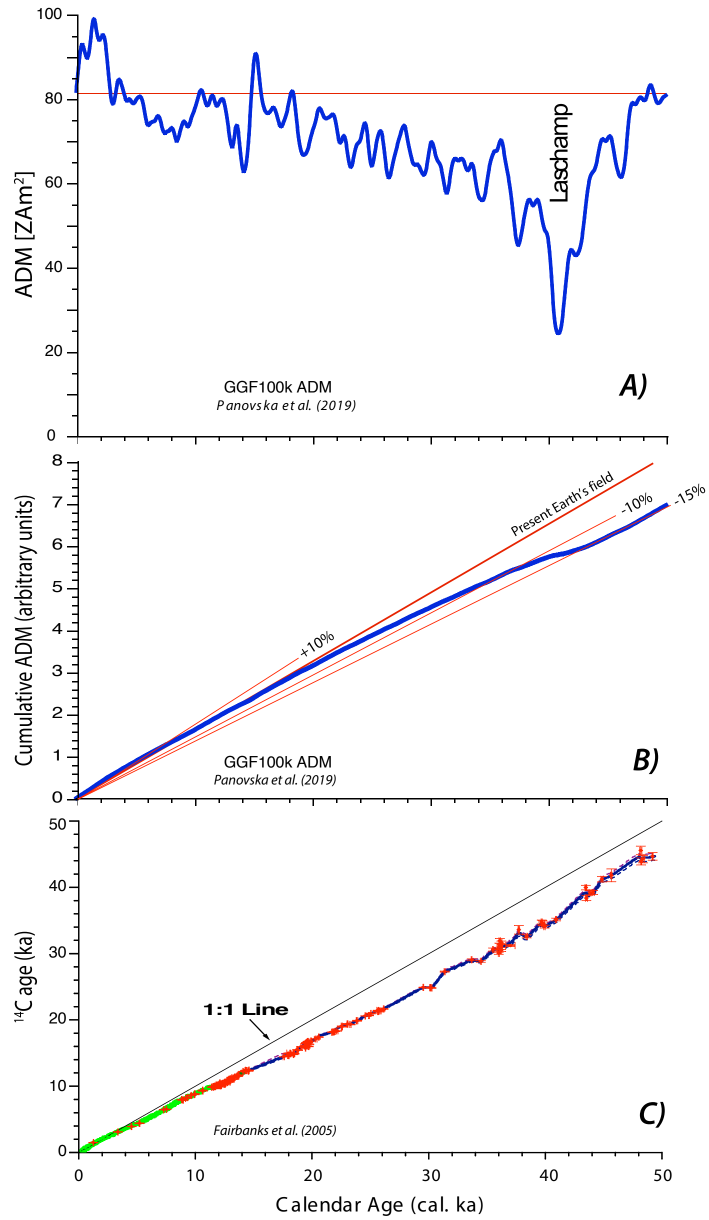

Fig. 7. A) Variations in geomagnetic axial dipole moment (ADM) for 0–50 cal. ka from Model GGF100k (blue wiggly line; Panovska et al., 2019). Present-day ADM is shown by horizontal line for reference. B) Cumulative ADM in 50-y intervals for Model GGF100k going back in time from the present (blue curve) and compared to cumulative ADM for a constant present Earth field dipole moment and for +10%, -10% and -15% of present Earth field dipole moment shown for reference (labeled red lines). C) Continuous calibration of high precision ^{14}C AMS dates to calendar ages based on U-series dates on corals and other calibration data from 0 to 50 cal. ka (from Fairbanks et al., 2005).

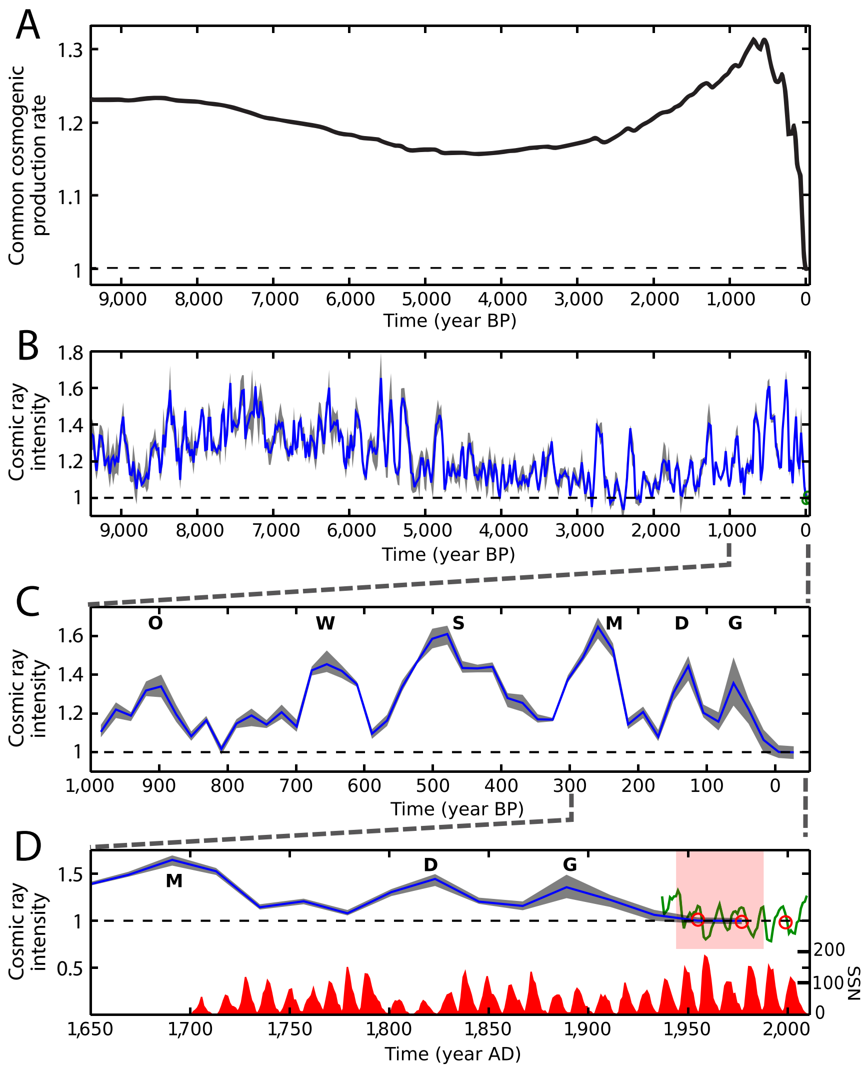

Fig. 8. Panel A shows time-integrated common production rate of cosmogenic radionuclides for the last 9400 cal. years relative to the present day (1944-1988 CE) from data shown in panel B that is zoomed in to past millennium (panel C) and to last 350 years (panel D). Panels B, C, and D are from Steinhilber et al. (2012) where red circles and green curve are 22-year averages and yearly averages of calculated cosmic ray intensity, and annual sunspot numbers (SSN) plotted at the bottom. Grand solar minima are O: Oort, W: Wolf, S: Spörer, M: Maunder, D: Dalton and G: Gleissberg. Black dashed lines in each panel represent average cosmic ray intensity for 1944-1988 CE. Data from Steinhilber et al. (2012)) is available at https://www.ncei.noaa.gov/pub/data/paleo/climate_forcing/solar_variability/steinhilber2012.txt.

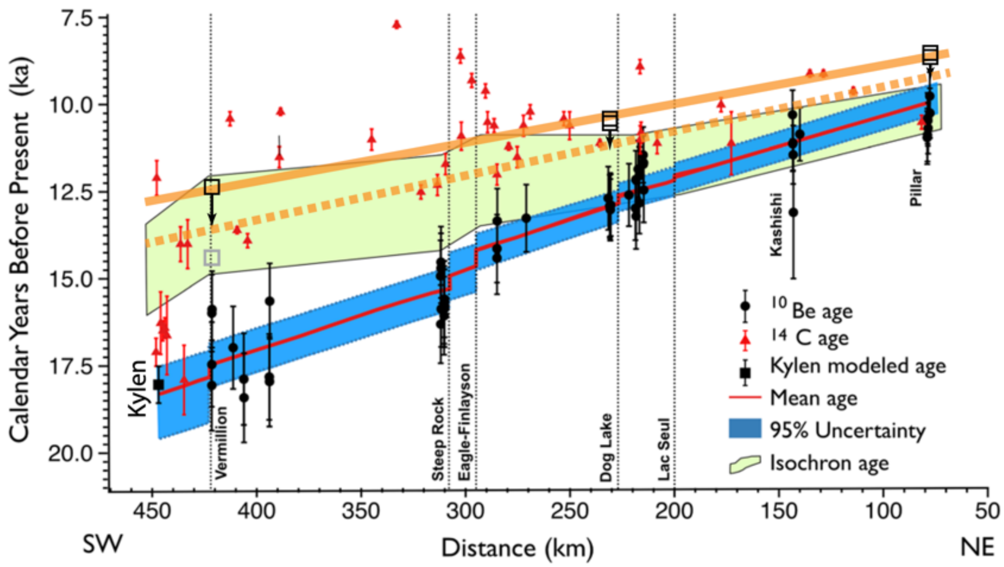

Fig. 9. Time-distance plot (adapted as base from Fig. 2 of (Lowell et al., 2021) with additions decribed below) showing chronological constraints on Laurentide Ice Sheet retreat along a transect from Kylen Lake (Minnesota) in SW to Pillar (Ontario) in NE (see **Fig. 1** for transect location). Red line with blue error envelope from Lowell et al. (2021) is their interpretation of retreat and hiatus pattern anchored to a ^{14}C bulk sediment mean basal age of 18.1 cal. ka at Kylen Lake and constrained by ^{10}Be exposure dates (black circles and error bars) using a SLHL ^{10}Be production rate of 4.33 at/g/y from Balco et al. (2009). Green shaded area is uncertainty envelope of radiocarbon-based isochrons of LIS retreat from Dalton et al. (2020) converted to calendar years by Lowell et al. (2021). Dark gray open squares are samples from Table S4 of Lowell et al. (2021) with ^{10}Be ages recalculated here with addition of a solar modulation factor of 1.23, which is equivalent to a SLHL ^{10}Be production rate of 5.3 at/g/y (implied retreat sketched as solid orange line), and scaled by an average of +8% using glacial isostatic adjustment model ICE-6G (Peltier et al., 2015) as implemented by (Jones et al., 2019) according to (Lowell et al., 2021) (implied retreat sketched as dashed orange line).

Table 1. Primary ^{10}Be calibration sites and Allamuchy site scaled with various schemes.

Parameters	Calibration				Allamuchy
	MR	PPT	SCOT	HU08	
Latitude, °N	-43.6	41.3	57.4	-13.9	41.0
Longitude, °E	170.6	-112.5	-5.6	70.9	-74.6
Altitude, m	1028	1603	136	4857	328
Air Pressure (ap), hPa	895.70	834.93	997.02	550.60	974.46
Atmospheric depth (x), g/cm2	913.35	851.38	1016.66	561.45	993.66
Number sampling sites	7	6	8	10	13
Cs (^{10}Be concentration), at/g	89900	257530	57274	559650	122000
Age, calendar years	9634	18300	11700	12300	TBD ↴
Ps (^{10}Be production rate), at/g/y	9.33	14.07	4.90	45.50	
St:					
S.lambda	2.351	3.525	1.161	12.410	1.276
M.lambda	1.556	1.968	1.069	4.265	1.103
F = S.lambda*M.lambda	2.330	3.484	1.159	12.198	1.272
C(SLHL): Cs/F, at/g	38584	73916	49428	45881	95913
P(SLHL): Cs/F/age, at/g/y	4.000	4.039	*4.224	3.730	*Age= 22707 cal. yr
P(SLHL+S): Cs/F*1.23/age, at/g/y	4.930	4.972	**5.201	4.592	**Age= 18441 cal. yr
GAD:					
Rc	4.479	5.303	1.356	14.069	5.414
f(Rc)	0.912	0.873	0.999	0.555	0.868
f(x)	2.457	3.882	1.134	26.461	1.340
F = f(Rc)*f(x)	2.241	3.390	1.133	14.673	1.163
C(SLHL): Cs/F, at/g	40116	75968	50537	38142	104863
P(SLHL): Cs/F/age, at/g/y	4.164	4.151	*4.320	3.101	*Age= 24274 cal. yr
P(SLHL+S): Cs/F*1.23/age, at/g/y	5.126	5.110	**5.317	3.814	**Age= 19722 cal. yr
SHA:					
Rc	5.209	5.721	1.583	13.139	5.595
f(Rc)	0.877	0.854	0.995	0.578	0.859
f(x)	2.445	3.868	1.134	26.972	1.340
F = f(Rc)*f(x)	2.143	3.303	1.128	15.599	1.150
C(SLHL): Cs/F, at/g	41950	77955	50787	35877	106052
P(SLHL): Cs/F/age, at/g/y	4.354	4.260	*4.341	2.917	*Age= 24430 cal. yr
P(SLHL+S): Cs/F*1.23/age, at/g/y	5.356	5.240	**5.339	3.843	**Age= 19864 cal. yr
TK03:					
Rc	5.833	6.439	2.842	13.493	6.618
f(Rc)	0.848	0.820	0.945	0.569	0.812
f(x)	2.433	3.835	1.132	26.772	1.336
F = f(Rc)*f(x)	2.064	3.145	1.069	15.235	1.100
C(SLHL): Cs/F, at/g	43556	81886	53544	36734	110918
P(SLHL): Cs/F/age, at/g/y	4.521	4.475	*4.576	2.987	*Age= 24239 cal. yr
P(SLHL+S): Cs/F*1.23/age, at/g/y	5.559	5.507	**5.629	3.663	**Age= 19705 cal. yr

^{10}Be exposure dating parameters for the CRONUS-Earth primary calibration sites from Borchers et al. (2016) (**Section S2**) used to derive ^{10}Be production rates normalized to sea level high altitude (SLHL) according to various scaling schemes: MR (Macaulay Ridge, NZ), PPT (Promontory Point Terrace, Utah), SCOT (Scotland), and HU08 (Huancane, Peru). Selected scaling schemes are St, the original empirical scaling scheme of Lal (1991) modified by Stone (2000); GAD, geocentric axial dipole where geographic and geomagnetic latitudes are equivalent in a static field; SHA, spherical harmonic model of 0-14 cal. ka paleomagnetic measurements (Pavón-Carrasco et al., 2014); TK03, statistical geomagnetic field model of Tauxe and Kent (2004). For GAD, SHA, and TK03, the effective vertical cutoff rigidity (Rc) is calculated using Equation 2 in Lifton et al. (2014), and the magnetic (f(Rc)), altitude (f(x)), and total scaling factor (F) are calculated using equations 6, 7 and 5, respectively, in Desilets et al. (2006). Geomagnetic dipole moment assumed to average to present-day value over exposure times less than ~20 cal. ka (see text). Also listed are published parameters for Allamuchy terminal moraine sites in New Jersey used to estimated ^{10}Be exposure age for retreat of Laurentide ice sheet (Corbett et al., 2017); ages for each scaling scheme based on asterisked production rates according to SCOT primary calibration data for reference; ages corresponding to other primary calibrations can be readily calculated.

Supplementary Material

Section S1. Various routines used for heuristic purposes relevant to ^{10}Be production rate scaling in the R programming language (R_Core_Team, 2018).

Section S2. CRONUS-Earth primary ^{10}Be calibration sample data (Borchers et al., 2016) as lodged in evolving versions of the ICE-D production rate online database (Martin et al., 2017). Items highlighted in yellow in attached pages generated by version 1 of the ICE-D infrastructure were used to calculate quantities shown in **Table 1.** According to the ICE-D document header, "As of April 2022, updates and corrections will only be made in version 2, and version 1 will no longer be updated." Hence including a copy of version 1 here is deemed useful for stability even though differences appear superficial with version 2 that currently (6/14/2023) resides at: https://version2.ice-d.org/production%20rate%20calibration%20data/cal_data_set/4.

Table S1. Effective vertical cutoff rigidity (R_c) and corresponding magnetic scaling factor ($f(R_c)$) as a function of latitude for various geomagnetic field models.

References

Borchers, B., Marrero, S., Balco, G., Caffee, M., Goehring, B., Lifton, N., Nishiizumi, K., Phillips, F., Schaefer, J., and Stone, J.: Geological calibration of spallation production rates in the CRONUS-Earth project, Quaternary Geochronology, 31, 188-198, https://doi.org/10.1016/j.quageo.2015.01.009, 2016.

Martin, L. C. P., Blard, P. H., Balco, G., Lavé, J., Delunel, R., Lifton, N., and Laurent, V.: The CREp program and the ICE-D production rate calibration database: A fully parameterizable and updated online tool to compute cosmic-ray exposure ages, Quaternary Geochronology, 38, 25-49, https://doi.org/10.1016/j.quageo.2016.11.006, 2017.

R_Core_Team: R: A language and environment for statistical computing, available at http://www.r-project.org [code], 2018.

```
########################## Cosmogenic Nuclide Funcs v4.2 ##########################
#
# https://www.r-project.org/
#

##
# Computes 10Be production rates according to Lal (1991)
# Earth and Planetary Science Letters, 104 (1991) 424-439
#
# L: geomagnetic latitude (deg)
# y: altitude (m)
#
lal.eq1 <- function(L, y){

  L <- abs(L)

  # altitude in km as in original formulation
  y <- y/1000

  ## Table 1 for 10Be
  A <- c(3.511, 3.360, 4.0607, 4.994, 5.594, 6.064, 5.594, 5.594)
  B <- c(2.547, 2.522, 2.734, 3.904, 4.946, 5.715, 6.018, 6.018)
  C <- c(0.95125, 1.0668, 1.2673, 0.9739, 1.3817, 1.6473, 1.7045, 1.7045)
  D <- c(0.18608, 0.18830, 0.22529, 0.42671, 0.53176, 0.68684, 0.71184, 0.71184)

  lam.bins <- c(0, 10, 20, 30, 40, 50, 60, 90)

  # interpolate coefficients to the Latitude (L)
  a <- approx(lam.bins, A, xout=L)$y
  b <- approx(lam.bins, B, xout=L)$y
  c <- approx(lam.bins, C, xout=L)$y
  d <- approx(lam.bins, D, xout=L)$y

  ## equation 1
  q <- a + b*y + c*y^2 + d*y^3

  return(q)
}


##
# Computes eq.2, eq. 3 and eq.4 from Stone (2000)
# JOURNAL OF GEOPHYSICAL RESEARCH, VOL. 105, NO. BlO, PAGES 23,753-23,759, OCTOBER 10, 2000
#
# Computes the altitude scaling factors (S.lambda)
# the rate of isotope production by muon capture (M.lambda)
# and the combined scaling factor (F.lambda) for 10Be
#
# ap:      atmospheric pressure (hPa)
# lambda:  magnetic latitude (deg)
#
stone.eq2 <- function(ap, lambda){

  lambda <- abs(lambda)

  # Stone (2000) Table 1
  A <- c(31.8518, 34.3699, 40.3153, 42.0983, 56.7733, 69.0720, 71.8733, 71.8733)
  B <- c(250.3193, 258.4759, 308.9894, 512.6857, 649.1343, 832.4566, 863.1927, 863.1927)
  C <- c(-0.083393, -0.089807, -0.106248, -0.120551, -0.160859, -0.199252, -0.207069, -0.207069)
```

```r
  D <- c(7.4260E-05, 7.9457E-05, 9.4508E-05, 1.1752E-04, 1.5463E-04, 1.9391E-04, 2.0127E-04,
 2.0127E-04)
  E <- c(-2.2397E-08, -2.3697E-08, -2.8234E-08, -3.8809E-08, -5.0330E-08, -6.3653E-08, -6.6043E-08,
 -6.6043E-08)
  M.1013 <- c(0.587, 0.600, 0.678, 0.833, 0.933, 1.000, 1.000, 1.000)

  lam.bins <- c(0, 10, 20, 30, 40, 50, 60, 90)

  # interpolate coefficients to the latitude (lambda)
  a <- approx(lam.bins, A, xout=lambda)$y
  b <- approx(lam.bins, B, xout=lambda)$y
  c <- approx(lam.bins, C, xout=lambda)$y
  d <- approx(lam.bins, D, xout=lambda)$y
  e <- approx(lam.bins, E, xout=lambda)$y
  M <- approx(lam.bins, M.1013, lambda)$y

  ## Altitude (atm. pressure) factor (eq.2)
  S.lambda <- a+b*exp(-ap/150)+c*ap+d*ap^2+e*ap^3

  ## Factor for isotope production by muon capture  (eq.3)
  M.lambda <- M * exp((1013.25 - ap)/242)

  # fraction of spallogenic production at sea level for 10Be
  f.sp <- 0.974

  ## Combined factor (eq.4)
  F.lambda <- f.sp * S.lambda + (1-f.sp) * M.lambda

  return(list(S.lambda = S.lambda, M.lambda = M.lambda, F.lambda = F.lambda))
}




##
# Computes vertical rigidity using eq.2 from Lifton et al. (2014)
# http://dx.doi.org/10.1016/j.epsl.2013.10.052
#
# lambda: magnetic latitude (deg)
# Mt:     the dipole moment at given time,
# Mo:     the reference dipole moment (2010 DGRF: 7.746e22 A m^2)
#
lifton.eq2 <- function(lambda, Mt=7.746, Mo = 7.746){

  lambda <- abs(lambda)

    l <- lambda/180*pi     # in radiants

    c1 <- 6.89901
    c2 <- 103.241
    c3 <- 522.061
    c4 <- 1152.15
    c5 <- 1189.18
    c6 <- 448.004

    Rc1 <-  (c1*cos(l) - c2*cos(l)^2 + c3*cos(l)^3 - c4*cos(l)^4 + c5*cos(l)^5 - c6*cos(l)^6)

    # rectify the "bouncing" at high latitudes
    zz <- which(lambda > 74.9)
    Rc1[zz] <- 0
```

```
    Rc <- (Mt/Mo) * Rc1

    return(Rc)
}



##
# Computes eq.6 and eq.7 from  Desilets et al. (2006)
# doi:10.1016/j.epsl.2006.03.051
#
# Computes the altitude scaling factors and
# scaling factor for the given magnetic rigidity.
# Total scaling factor is the product of the 2 factors
#
# ap: atmospheric pressure (hPa)
# Rc: rigidity (GV)
#
desilets.eq7 <- function(ap = 1013.25, Rc = 0){

  # convert hPa to gr/cm^2
  x <- ap * 1.0197

  # Desilets et al 2006 eq.6 (i.e., Dorman function)
  alpha <- 10.275
  kappa <- 0.9615
  f.Rc <- 1 - exp(-alpha * Rc^(-kappa))

  # coefficients from Table 2
  n   <- 1.0177E-02
  a   <- 1.0207E-01
  k   <- -3.9527E-01
  a0  <- 8.5236E-06
  a1  <- -6.3670E-07
  a2  <- -7.0814E-09
  a3  <- -9.9182E-09
  a4  <- 9.9250E-10
  a5  <- 2.4925E-11
  a6  <- 3.8615E-12
  a7  <- -4.8194E-13
  a8  <- -1.5371E-14

  ## polynomial coefficients of eq.5 and eq.7
  #  note that c3 and c4 are negligible for any reasonable value of Rc
  c1 <- n/(1 + exp(-a * Rc^(-k)))
  c2 <- (a0 + a1*Rc + a2*Rc^2)/2
  c3 <- (a3 + a4*Rc + a5*Rc^2)/3
  c4 <- (a6 + a7*Rc + a8*Rc^2)/4

  # polynomial values for 1033 g/cm2 and site pressure
  p.1033 <- c1*1033 + c2*1033^2 + c3*1033^3 + c4*1033^4
  p.x    <- c1*x + c2*x^2 + c3*x^3 + c4*x^4

  # Desilets et al 2006  eq.5
  lambda.1033 <- (1033 - x) / (p.1033 - p.x)

  ## Desilets et al. (2006) eq.7 (also eq. 2 of Desilets and Zreda, 2003)
  #  note that this equation has typos in Desilets et al. (2006)
  f.x  <- exp((1033 - x)/lambda.1033)
```

```
  return(list(mag.factor=f.Rc, alt.factor=f.x, Total.factor=f.Rc * f.x))
}



##
# Computes the averaged 10Be production factor from Steinhilber et al. 2012
# doi:10.1073/pnas.1118965109
#
# Need file "steinhilber2012_TSI.txt" in the working folder
# ftp://ftp.ncdc.noaa.gov/pub/data/paleo/climate_forcing/solar_variability/steinhilber2012.txt
#
# age: age  (yr BP)
#
# Returns the inverse of Steinhilber's production rate averaged between
# today and the given age.
#
# For instance:
# steinhilber.pf(1000) returns a production factor pf = 0.7863477,
# meaning that present day production is 0.7863477 times the averaged
# production of the last 1000 years, hence averaged production in the
# last 1000 yr was almost 30% larger than present day production.
#
steinhilber.pf <- function(age){

  if(age > 9389) {
    warning("steinhilber.pf: age too old, production factor = 1/1.231\n")
    pr <- 1.231
  } else {
    dat <- read.table("steinhilber2012_TSI.txt",
                      header = TRUE,
                      skip = 156)

    idx <- which(dat$Year < age)
    pr <- mean(dat$X1.PC[idx])
  }
  return(sf=1/pr)
}


##
# Computes total cosmogenic production factor with constant geocentric axial dipole
# (GAD) field, air pressure and age (age is used only to include the variability of
# production rate from Steinhilber et al. 2012).
#
# Combines lifton.eq2, desilets.eq7, and Steinhilber (2012) data (if age is given).
# By default the "steinhilber factor" is disregarded (i.e. set to 1).
# If age > 9400 the steinhilber factor is set to 1/1.231 (with a warning message)
#
# lambda: magnetic latitude (deg)
# ap:  air pressure (hPa)
# age: age (yrBP) - default NA i.e., no steinhilber correction
# ...: additional arguments passed to lifton.eq2 (e.g. virtual dipole moment Mt)
#
cosmogenic.factor.GAD <- function(ap=1013.25, lambda, age = NA, ...){

  Rc <- lifton.eq2(lambda, ...)
  df <- desilets.eq7(ap, Rc=Rc)
```

```
  if (is.na(age)){
    sf <- 1
  } else {
    sf <- steinhilber.pf(age)
  }

  return(list(mag.factor = df$mag.factor,
              alt.factor = df$alt.factor,
              solar.factor = sf,
              total.factor=df$mag.factor * df$alt.factor * sf))
}




##
# Computes total cosmogenic factor with the GAD hypothesis
# and the variable Axial Dipole Moment (ADM) of Panovska et al. (2019)
#
# Combines lifton.eq2, desilets.eq7 using ADM from
# Panovska S., Korte M., & Constable C. G. (2019).
# https://doi.org/10.1029/ 2019RG000656
#
# It needs the following file in the working directory:
# (downloaded from https://earthref.org/ERDA/2384/)
# "ADM_GGF100k.txt"
#
# lambda: magnetic latitude (deg)
# ap:  air pressure (hPa) - default 1013.25
# age: age (yrBP)
# Mo:  present day geomagnetic dipole moment (1e22 A m^2) - default 7.746
#
cosmogenic.factor.ADM <- function(ap = 1013.25, lambda, age, Mo = 7.746){

  age <- age/1000  # age in kyr
  if(age > 100){stop("Age must be smaller than 100 kyrBP")}

  adm <- read.table("ADM_GGF100k.txt", header = FALSE, skip = 1)

  idx <- which(adm$V1 <= age)

  ## Compute Rc and df for all ages
  Rcs <- lifton.eq2(lambda, Mt = adm$V2[idx], Mo = Mo)
  df <- desilets.eq7(ap, Rc=Rcs)

  ## return the average values (i.e., integrate through time)
  mag.factor <- mean(df$mag.factor)
  alt.factor <- mean(df$alt.factor)
  Rc <- mean(Rcs)

  return(list(mean.Rc=Rc, mag.factor=mag.factor, alt.factor=alt.factor, total.factor=mag.factor *
 alt.factor))
}




##
# Computes total cosmogenic factor using geomagnetic latitude and field intensity
# from the SHA.DIF.14k geomagnetic model, air pressure and age < 14000 yr BP.
```

```
#  The Steinhilber production factor can be included for ages < 9400 yr BP
#
# Needs the following files in the working directory:
# "coeff_SHA.DIF.14k.dat"
# "steinhilber2012_TSI.txt" (if steinhilber = TRUE)
#
# ap:          air pressure (hPa) - default 1013.25
# lat:         geographic latitude (deg)
# long:        geographic longitude (deg) - default 0
# age:         age (yrBP) - must be < 14000
# steinhilber: if TRUE includes the variability of production rate - default FALSE
# dir.only:    if TRUE ignore field intensity - default FALSE
#
cosmogenic.factor.SHAdif <- function(ap = 1013.25,
                                     lat,
                                     long = 0,
                                     age,
                                     steinhilber = FALSE,
                                     dir.only = FALSE)
  {


  if (age > 14000){
    warning("cosmogenic.factor.SHAdif: calculation is inaccurate for age > 14000\n")
  }

  # SHA.DIF.14k uses ages in yrAD
  ageAD <- 1950 - age

  ## This is the complete dataset of Gauss coefficient from file "sha-dif-14k.rar"
  #  (downloaded it from https://earthref.org/ERDA/1897/)
  #
  ## read SHA table of sha_dif_14k
  sha <- read.table("coeff_SHA.DIF.14k.dat", header = T)

  ## select only dipole coefficients
  tmp1 <- subset(sha, subset = order == 1 & rank == 0, select = c(Age, g0=g))
  tmp2 <- subset(sha, subset = order == 1 & rank == 1, select = c(g, h))
  sha.dipole<-data.frame(Age = tmp1$Age, g01 = tmp1$g, g11 = tmp2$g, h11 = tmp2$h)

  ## compute dipole axis from Gauss dipolar coefficients
  dipole <- gauss2dipole(sha.dipole$g01, sha.dipole$g11, sha.dipole$h11)
  dipole$Age <- sha.dipole$Age

  site <- c(long, lat)

  # select relevant ages (AD)
  idx <- which(ageAD <= dipole$Age)

  # Magnetic colatitude of site is the angle (great circle distance) between magnetic pole and site
  Mlat <- 90 - angle(cbind(dipole$phi[idx], 90-dipole$theta[idx]), site, all=T)

  idx2 <- which(Mlat >90)
  Mlat[idx2] <- 180-Mlat[idx2]

  if (dir.only){
    # disregards the variability of dipole intensity
    Rcs <- lifton.eq2(lambda = Mlat)
  } else {
    # direction and intensity (Mo = 30.1 µT from IGRF2000)
```

```
    Rcs <- lifton.eq2(lambda = Mlat, Mt = dipole$Bo[idx], Mo = 30.1)
  }

  df <- desilets.eq7(ap, Rc=Rcs)

  mf <- mean(df$mag.factor)  # mean magnetic factor
  af <- mean(df$alt.factor)  # mean altitude factor
  Rc <- mean(Rcs)            # mean Rc

  if (steinhilber){
    sf <- steinhilber.pf(age)
  } else {
    sf <- 1
  }

  return(list(mean.Rc=Rc, mag.factor=mf, alt.factor=af, solar.factor=sf, total.factor=mf * af * sf))
}



##
# Computes total cosmogenic factor using the geomagnetic latitudes
# from TK03 geomagnetic model and air pressure
#
#  ** It needs pmag.py installed to compute the TK03 dataset **
#  https://pmagpy.github.io/PmagPy-docs/intro.html
#
#
# ap:   air pressure (hPa) - default 1013.25
# lat:  site latitude (deg)
# ...:  additional arguments passed to lifton.eq2 (e.g. virtual dipole moment Mt)
#
cosmogenic.factor.TK03 <- function(ap = 1013.25, lat, ...){

  ## compose the command string to run tk03.py
  # this makes 5000 surrogates and store in temporary file named tk03.tmp
  # command string will be: tk03.py -n 5000 -lat xx  > tk03.tmp
  cmd.str <- paste("tk03.py -n 5000 -lat ", lat)
  cmd.str <- paste(cmd.str, "> tk03.tmp")

  ## loop the multiple command strings (i.e., lat)
  #  for each cmd.str compute the Rc
  r <- length(cmd.str)
  mf <- mat.or.vec(nr = r, nc = 1)
  af <- mat.or.vec(nr = r, nc = 1)
  mRc <- mat.or.vec(nr = r, nc = 1)
  for (l in 1:r){
    system(cmd.str[l])
    TK03 <- read.table("tk03.tmp", skip = 7) # skip = 7 remove some warning lines in my computer

    pole <- vgp(TK03[, 1:2], lat[l], 0)
    Mlat <- 90 - angle(cbind(pole[,2], pole[,1]), c(0, lat[l]), all=T) # pls note that latitudes can be
 negative

    # compute vertical rigidities
    Rc <- lifton.eq2(Mlat)

    # compute scaling factors
    df <- desilets.eq7(ap, Rc=Rc)
```

```
    mf[l] <- mean(df$mag.factor)  # mean magnetic factor
    af[l] <- mean(df$alt.factor)  # mean altitude factor
    mRc[l] <- mean(Rc)

  }

  # make a table with results
  results <- data.frame(Command.string = cmd.str,
                        latitude = lat,
                        mean.Rc = mRc,
                        mag.factor = mf,
                        alt.factor = af,
                        total.factor = mf * af)

  # remove the temporary file
  system("rm tk03.tmp")

  return(results)
}



##
# conversion from height or altitude (meters, m), to air pressure (hPa) at temperature = 15 C
h2p <- function(h) {
  ap <- 101325 * (1 - 2.25577e-5 * h)^5.25588
  return(ap/100)
}



##
# Compute the dipole axis direction and Bo given the Gauss coefficient of order 1
#
gauss2dipole <- function(g01, g11, h11){
  Bo <- sqrt(g01^2 + g11^2 + h11^2)
  c1 <- sqrt(g11^2 + h11^2)

  theta <- acos(-g01/Bo) *180/pi
  phi <- acos(-g11/c1) *180/pi

  idx <- which(h11 > 0)
  phi[idx] <- -phi[idx] + 360

  return(list(theta = theta, phi = phi, Bo = Bo))
}


##
# angle between directions dir1 and dir2, in deg
angle <- function(dir1, dir2, all = FALSE){

  P1 <- ai_lmn(dir1)
  P2 <- ai_lmn(dir2)
  A <- acos(P1 %*% t(P2))*180/pi

  if(!all) {A <- diag(A)}

  return(A)
}
```

```
##
# from azimuth and anclination to directors cosine
ai_lmn <- function(di){
  di <- as.matrix(di)
  if(ncol(di) == 1) {di <- t(di)}
  di <- di*pi/180   # in rad

  l <-cos(di[,2]) * cos(di[,1])
  m <-cos(di[,2]) * sin(di[,1])
  n <-sin(di[,2])

  lmn <- cbind(l, m, n)
  colnames(lmn) <- c("l", "m", "n")
  return(lmn)
}


##
#  Calculate the (Virtual) Geomagnetic Pole given the site coordinates
#  and the (paleo)magnetic direction.
#  Angles are in deg.
#  dir: column matrix with declination and inclination
#
vgp <- function(dir,  site.lat,  site.long)
{

  dec <- dir[,1]
  inc <- dir[,2]
  r <- pi/180

  P <- atan2(2, tan(inc*r)) # magnetic colatitude in radiants

  # Buttler eq: 7.2 (radiants)
  vgp.lat <- asin(sin(site.lat*r)*cos(P) + cos(site.lat*r)*sin(P)*cos(dec*r))

  # Buttler eq: 7.3
  a <-round((sin(P)*sin(dec*r))/cos(vgp.lat), 10)
  beta <- asin(a)*180/pi

  vgp.long <- site.long + 180 - beta
  idx <- which(cos(P) >= (sin(site.lat*r)*sin(vgp.lat)))
  vgp.long[idx] <-site.long+beta[idx]      # overwrite condition above

  vgp.lat <- vgp.lat *180/pi  # VGPlat in deg

  return(cbind(lat = vgp.lat, long = vgp.long))
}
```

ICE-D informal cosmogenic-nuclide exposure-age database — PRODUCTION RATE CALIBRATION DATA

Note: This page is generated by version 1 of the ICE-D infrastructure and will soon be replaced by an updated version that is under development at **version2.ice-d**
As of April 2022, updates and corrections will only be made in version 2, and version 1 will no longer be updated.

Calibration data set: CRONUS - Primary Be-10 - 2015: Be-10

CRONUS-Earth "Primary" Be-10 calibration data set of Borchers et al. (2015).

Associated publication:

Borchers, Brian; Marrero, Shasta; Balco, Greg; Caffee, Marc; Goehring, Brent; Lifton, Nathaniel; Nishiizumi, Kunihiko; Phillips, Fred; Schaefer, Joerg; Stone,
Geological calibration of spallation production rates in the CRONUS-Earth Project
Quaternary Geochronology, 2015

Sample name	Latitude (DD)	Longitude (DD)	Elevation (m)	Lithology	What is it?	Site	^{10}Be (qtz)	^{26}Al (qtz)	^{14}C (qtz)
MR-08-05	-43.57435	170.60760	1032	Greywacke sandstone	Boulder	MACAULAY	1		
MR-08-04	-43.57444	170.60832	1028	Greywacke sandstone	Boulder	MACAULAY	1		
MR-08-03	-43.57452	170.60805	1029	Greywacke sandstone	Boulder	MACAULAY	1		
MR-08-02	-43.57581	170.60857	1025	Greywacke sandstone	Boulder	MACAULAY	1		
MR-08-01	-43.57605	170.60835	1025	Greywacke sandstone	Boulder	MACAULAY	1		
MR-08-13	-43.57751	170.60695	1028	Greywacke sandstone	Boulder	MACAULAY	1		
MR-08-14	-43.57787	170.60493	1032	Greywacke sandstone	Boulder	MACAULAY	1		
06-SKY-01	57.24081	-5.97272	442	Quartzite	Glacially transported boulder	FEAR	2		
06-SKY-03	57.24091	-5.96811	323	Quartzite	Glacially transported boulder	FEAR	2	1	
06-SKY-04	57.24223	-5.96876	339	Quartzite	Glacially transported boulder	FEAR	2		
06-SKY-05	57.24240	-5.96630	322	Quartzite	Glacially transported boulder	FEAR	1		
06-SKY-06	57.24249	-5.96588	310	Quartzite	Glacially transported boulder	FEAR	2		
06-SKY-07	57.24269	-5.96485	300	Quartzite	Glacially transported boulder	FEAR	2	1	
06-SKY-08	57.24250	-5.96530	314	Quartzite	Glacially transported boulder	FEAR	1		
06-HKY-05	57.48742	-5.44928	521	Quartzite	Glacially transported boulder	MCD	1	1	
06-HKY-06	57.48755	-5.44977	527	Quartzite	Glacially transported boulder	MCD	1	1	
06-HKY-07	57.48778	-5.44772	500	Quartzite	Glacially transported boulder	MCD	1	1	
06-HKY-08	57.48868	-5.44703	502	Quartzite	Glacially transported boulder	MCD	1	1	
06-HKY-10	57.48732	-5.44866	510	Quartzite	Glacially transported boulder	MCD	1	1	
06-HKY-11	57.48743	-5.44989	528	Quartzite	Glacially transported boulder	MCD	1	1	
02-SCOT-001-ARR	57.41413	-5.64375	139	Arkosic metasandstone	Glacially transported boulder	ARR	1	1	
02-SCOT-002-ARR	57.41413	-5.64375	139	Arkosic metasandstone	Glacially transported boulder	ARR	1	1	
02-SCOT-003-ARR	57.41413	-5.64375	139	Arkosic metasandstone	Glacially transported boulder	ARR	1		
02-SCOT-004-ARR	57.41512	-5.64620	135	Arkosic metasandstone	Glacially transported boulder	ARR	1	1	
02-SCOT-005-ARR	57.41512	-5.64620	135	Arkosic metasandstone	Glacially transported boulder	ARR	1	1	
02-SCOT-006-ARR	57.41525	-5.64641	133	Arkosic metasandstone	Glacially transported boulder	ARR	1	1	
02-SCOT-007-ARR	57.41525	-5.64641	133	Arkosic metasandstone	Glacially transported boulder	ARR	1	1	
02-SCOT-008-ARR	57.41525	-5.64641	133	Arkosic metasandstone	Glacially transported boulder	ARR	1	1	
06-HKY-01	57.41525	-5.64641	133	Arkosic metasandstone	Glacially transported boulder	ARR	1	1	
06-HKY-03A	57.41550	-5.64662	131	Arkosic metasandstone	Glacially transported boulder	ARR	1	1	
06-HKY-04	57.42309	-5.65812	137	Arkosic metasandstone	Glacially transported boulder	ARR	1	1	
05-PPT-01	41.26367	-112.47527	1603	Quartzite	Bedrock	PPT	6	4	
05-PPT-02	41.26367	-112.47527	1603	Quartzite	Bedrock	PPT	6	4	
05-PPT-03	41.26356	-112.47580	1600	Quartzite	Bedrock	PPT	7	5	
05-PPT-04	41.26362	-112.47693	1598	Quartzite	Bedrock	PPT	7	4	
05-PPT-05	41.26390	-112.47498	1605	Quartzite	Bedrock	PPT	7	5	
05-PPT-08	41.26379	-112.47476	1606	Quartzite	Bedrock	PPT	6	3	
HU08-01	-13.94494	-70.89539	4854	Rhyolitic ignimbrite	Moraine boulder	HUANCANE2A	4	1	
HU08-02	-13.94635	-70.89241	4862	Rhyolitic ignimbrite	Moraine boulder	HUANCANE2A	4	1	
HU08-03	-13.94613	-70.89266	4859	Rhyolitic ignimbrite	Moraine boulder	HUANCANE2A	2	1	
HU08-04	-13.94545	-70.89280	4848	Rhyolitic ignimbrite	Moraine boulder	HUANCANE2A	3	1	

HU08-06	-13.94454	-70.89483	4843	Rhyolitic ignimbrite	Moraine boulder	HUANCANE2A	3	1
HU08-10	-13.94700	-70.88693	4860	Rhyolitic ignimbrite	Moraine boulder	HUANCANE2A	3	1
HU08-11	-13.94715	-70.88680	4860	Rhyolitic ignimbrite	Moraine boulder	HUANCANE2A	2	1
HU08-14	-13.94887	-70.88559	4871	Rhyolitic ignimbrite	Moraine boulder	HUANCANE2A	2	1
HU08-15	-13.94838	-70.88537	4869	Rhyolitic ignimbrite	Moraine boulder	HUANCANE2A	2	1
HU08-16	-13.94679	-70.88619	4867	Rhyolitic ignimbrite	Moraine boulder	HUANCANE2A	2	1

Online calculator input, version 3:

This can be entered in the v3 production rate calibration input page.
Nuclide concentrations not relevant to this calibration data set have been stripped out of the text block.

```
MR-08-05 -43.57435 170.60760 1032 std  1.6 2.74 0.9910 0.00e+00 2008;
MR-08-05 true_t MACAULAY 9634 50;
MR-08-05 Be-10 quartz 8.970e+04 2.400e+03 07KNSTD;
MR-08-04 -43.57444 170.60832 1028 std  0.8 2.75 0.9890 0.00e+00 2008;
MR-08-04 true_t MACAULAY 9634 50;
MR-08-04 Be-10 quartz 8.860e+04 2.200e+03 07KNSTD;
MR-08-03 -43.57452 170.60805 1029 std  1.9 2.74 0.9880 0.00e+00 2008;
MR-08-03 true_t MACAULAY 9634 50;
MR-08-03 Be-10 quartz 8.780e+04 1.700e+03 07KNSTD;
MR-08-02 -43.57581 170.60857 1025 std  1.0 2.74 0.9930 0.00e+00 2008;
MR-08-02 true_t MACAULAY 9634 50;
MR-08-02 Be-10 quartz 9.170e+04 2.600e+03 07KNSTD;
MR-08-01 -43.57605 170.60835 1025 std  0.8 2.74 0.9920 0.00e+00 2008;
MR-08-01 true_t MACAULAY 9634 50;
MR-08-01 Be-10 quartz 8.750e+04 1.900e+03 07KNSTD;
MR-08-13 -43.57751 170.60695 1028 std  1.7 2.71 0.9910 0.00e+00 2008;
MR-08-13 true_t MACAULAY 9634 50;
MR-08-13 Be-10 quartz 8.960e+04 1.800e+03 07KNSTD;
MR-08-14 -43.57787 170.60493 1032 std  2.2 2.73 0.9910 0.00e+00 2008;
MR-08-14 true_t MACAULAY 9634 50;
MR-08-14 Be-10 quartz 8.810e+04 1.700e+03 07KNSTD;
06-SKY-01 57.24081 -5.97272 442 std  7.0 2.52 0.9240 0.00e+00 2006;
06-SKY-01 true_t FEAR 11700 300;
06-SKY-01 Be-10 quartz 7.089e+04 2.428e+03 07KNSTD;
06-SKY-01 Be-10 quartz 7.318e+04 6.827e+03 07KNSTD;
06-SKY-03 57.24091 -5.96811 323 std  8.0 2.52 0.9580 0.00e+00 2006;
06-SKY-03 true_t FEAR 11700 300;
06-SKY-03 Be-10 quartz 6.269e+04 1.953e+03 07KNSTD;
06-SKY-03 Be-10 quartz 6.185e+04 4.655e+03 07KNSTD;
06-SKY-04 57.24223 -5.96876 339 std  7.5 2.46 0.9760 2.14e-05 2006;
06-SKY-04 true_t FEAR 11700 300;
06-SKY-04 Be-10 quartz 6.786e+04 1.895e+03 07KNSTD;
06-SKY-04 Be-10 quartz 7.476e+04 7.543e+03 07KNSTD;
06-SKY-05 57.24240 -5.96630 322 std  3.5 2.44 0.9870 2.14e-05 2006;
06-SKY-05 true_t FEAR 11700 300;
06-SKY-05 Be-10 quartz 7.007e+04 9.006e+03 07KNSTD;
06-SKY-06 57.24249 -5.96588 310 std  7.5 2.49 0.9900 2.14e-05 2006;
06-SKY-06 true_t FEAR 11700 300;
06-SKY-06 Be-10 quartz 6.588e+04 2.089e+03 07KNSTD;
06-SKY-06 Be-10 quartz 7.026e+04 7.114e+03 07KNSTD;
06-SKY-07 57.24269 -5.96485 300 std  6.0 2.56 0.9920 2.14e-05 2006;
06-SKY-07 true_t FEAR 11700 300;
06-SKY-07 Be-10 quartz 6.425e+04 2.133e+03 07KNSTD;
06-SKY-07 Be-10 quartz 6.456e+04 4.951e+03 07KNSTD;
06-SKY-08 57.24250 -5.96530 314 std  2.0 2.41 0.9880 0.00e+00 2006;
06-SKY-08 true_t FEAR 11700 300;
06-SKY-08 Be-10 quartz 6.410e+04 4.194e+03 07KNSTD;
06-HKY-05 57.48742 -5.44928 521 std  4.0 2.55 0.9870 0.00e+00 2006;
06-HKY-05 true_t MCD 11700 300;
06-HKY-05 Be-10 quartz 8.114e+04 1.416e+03 07KNSTD;
06-HKY-06 57.48755 -5.44977 527 std  3.8 2.53 0.9870 0.00e+00 2006;
06-HKY-06 true_t MCD 11700 300;
06-HKY-06 Be-10 quartz 8.261e+04 2.545e+03 07KNSTD;
06-HKY-07 57.48778 -5.44772 500 std  6.2 2.59 0.9890 0.00e+00 2006;
06-HKY-07 true_t MCD 11700 300;
06-HKY-07 Be-10 quartz 7.793e+04 1.519e+03 07KNSTD;
06-HKY-08 57.48868 -5.44703 502 std  4.0 2.59 0.9880 0.00e+00 2006;
06-HKY-08 true_t MCD 11700 300;
06-HKY-08 Be-10 quartz 7.956e+04 1.320e+03 07KNSTD;
06-HKY-10 57.48732 -5.44866 510 std  6.8 2.59 0.9870 0.00e+00 2006;
06-HKY-10 true_t MCD 11700 300;
06-HKY-10 Be-10 quartz 7.856e+04 1.408e+03 07KNSTD;
06-HKY-11 57.48743 -5.44989 528 std  4.0 2.58 0.9870 0.00e+00 2006;
06-HKY-11 true_t MCD 11700 300;
06-HKY-11 Be-10 quartz 8.380e+04 1.235e+03 07KNSTD;
```

```
02-SCOT-001-ARR 57.41413 -5.64375 139 std  4.0 2.57 0.9900 1.03e-04 2002;
02-SCOT-001-ARR true_t ARR 11700 300;
02-SCOT-001-ARR Be-10 quartz 5.652e+04 1.266e+03 07KNSTD;
02-SCOT-002-ARR 57.41413 -5.64375 139 std  2.0 2.57 0.9900 1.03e-04 2002;
02-SCOT-002-ARR true_t ARR 11700 300;
02-SCOT-002-ARR Be-10 quartz 5.742e+04 1.143e+03 07KNSTD;
02-SCOT-003-ARR 57.41413 -5.64375 139 std  4.0 2.57 0.9900 1.03e-04 2002;
02-SCOT-003-ARR true_t ARR 11700 300;
02-SCOT-003-ARR Be-10 quartz 5.435e+04 1.232e+03 07KNSTD;
02-SCOT-004-ARR 57.41512 -5.64620 135 std  6.2 2.71 0.9880 1.03e-04 2002;
02-SCOT-004-ARR true_t ARR 11700 300;
02-SCOT-004-ARR Be-10 quartz 5.748e+04 1.164e+03 07KNSTD;
02-SCOT-005-ARR 57.41512 -5.64620 135 std  3.3 2.57 0.9880 1.03e-04 2002;
02-SCOT-005-ARR true_t ARR 11700 300;
02-SCOT-005-ARR Be-10 quartz 5.884e+04 1.314e+03 07KNSTD;
02-SCOT-006-ARR 57.41525 -5.64641 133 std  2.4 2.57 0.9880 1.03e-04 2002;
02-SCOT-006-ARR true_t ARR 11700 300;
02-SCOT-006-ARR Be-10 quartz 5.635e+04 1.988e+03 07KNSTD;
02-SCOT-007-ARR 57.41525 -5.64641 133 std  2.1 2.57 0.9880 1.03e-04 2002;
02-SCOT-007-ARR true_t ARR 11700 300;
02-SCOT-007-ARR Be-10 quartz 5.952e+04 1.688e+03 07KNSTD;
02-SCOT-008-ARR 57.41525 -5.64641 133 std  1.4 2.57 0.9880 1.03e-04 2002;
02-SCOT-008-ARR true_t ARR 11700 300;
02-SCOT-008-ARR Be-10 quartz 5.772e+04 1.151e+03 07KNSTD;
06-HKY-01 57.41525 -5.64641 133 std  2.5 2.52 0.9880 1.03e-04 2006;
06-HKY-01 true_t ARR 11700 300;
06-HKY-01 Be-10 quartz 5.739e+04 1.207e+03 07KNSTD;
06-HKY-03A 57.41550 -5.64662 131 std  5.8 2.47 0.9850 1.03e-04 2006;
06-HKY-03A true_t ARR 11700 300;
06-HKY-03A Be-10 quartz 6.205e+04 1.180e+03 07KNSTD;
06-HKY-04 57.42309 -5.65812 137 std  10.0 2.59 0.9720 0.00e+00 2006;
06-HKY-04 true_t ARR 11700 300;
06-HKY-04 Be-10 quartz 5.331e+04 1.026e+03 07KNSTD;
05-PPT-01 41.26367 -112.47527 1603 std  3.0 2.65 0.9780 0.00e+00 2005;
05-PPT-01 true_t PPT 18300 300;
05-PPT-01 Be-10 quartz 2.542e+05 3.743e+03 07KNSTD;
05-PPT-01 Be-10 quartz 2.394e+05 5.166e+03 07KNSTD;
05-PPT-01 Be-10 quartz 2.495e+05 3.992e+03 07KNSTD;
05-PPT-01 Be-10 quartz 2.840e+05 7.324e+03 KNSTD;
05-PPT-01 Be-10 quartz 2.526e+05 4.516e+03 07KNSTD;
05-PPT-01 Be-10 quartz 2.658e+05 6.240e+03 07KNSTD;
05-PPT-02 41.26367 -112.47527 1603 std  3.0 2.65 0.9940 0.00e+00 2005;
05-PPT-02 true_t PPT 18300 300;
05-PPT-02 Be-10 quartz 2.594e+05 3.411e+03 07KNSTD;
05-PPT-02 Be-10 quartz 2.363e+05 5.136e+03 07KNSTD;
05-PPT-02 Be-10 quartz 2.408e+05 5.058e+03 07KNSTD;
05-PPT-02 Be-10 quartz 2.822e+05 7.533e+03 KNSTD;
05-PPT-02 Be-10 quartz 2.467e+05 4.581e+03 07KNSTD;
05-PPT-02 Be-10 quartz 2.483e+05 5.025e+03 07KNSTD;
05-PPT-03 41.26356 -112.47580 1600 std  3.5 2.65 0.9620 0.00e+00 2005;
05-PPT-03 true_t PPT 18300 300;
05-PPT-03 Be-10 quartz 2.490e+05 3.452e+03 07KNSTD;
05-PPT-03 Be-10 quartz 2.435e+05 3.276e+03 07KNSTD;
05-PPT-03 Be-10 quartz 2.390e+05 5.693e+03 07KNSTD;
05-PPT-03 Be-10 quartz 2.503e+05 7.758e+03 07KNSTD;
05-PPT-03 Be-10 quartz 2.859e+05 6.159e+03 KNSTD;
05-PPT-03 Be-10 quartz 2.483e+05 4.428e+03 07KNSTD;
05-PPT-03 Be-10 quartz 2.552e+05 6.736e+03 07KNSTD;
05-PPT-04 41.26362 -112.47693 1598 std  2.5 2.66 0.9820 0.00e+00 2005;
05-PPT-04 true_t PPT 18300 300;
05-PPT-04 Be-10 quartz 2.539e+05 4.307e+03 07KNSTD;
05-PPT-04 Be-10 quartz 2.424e+05 4.710e+03 07KNSTD;
05-PPT-04 Be-10 quartz 2.456e+05 4.175e+03 07KNSTD;
05-PPT-04 Be-10 quartz 2.521e+05 4.286e+03 07KNSTD;
05-PPT-04 Be-10 quartz 2.942e+05 6.595e+03 KNSTD;
05-PPT-04 Be-10 quartz 2.481e+05 5.374e+03 07KNSTD;
05-PPT-04 Be-10 quartz 2.567e+05 6.602e+03 07KNSTD;
05-PPT-05 41.26390 -112.47498 1605 std  4.0 2.67 0.9900 0.00e+00 2005;
05-PPT-05 true_t PPT 18300 300;
05-PPT-05 Be-10 quartz 2.751e+05 5.399e+03 07KNSTD;
05-PPT-05 Be-10 quartz 2.470e+05 3.331e+03 07KNSTD;
05-PPT-05 Be-10 quartz 2.541e+05 4.319e+03 07KNSTD;
05-PPT-05 Be-10 quartz 2.492e+05 5.385e+03 07KNSTD;
05-PPT-05 Be-10 quartz 2.803e+05 6.617e+03 KNSTD;
05-PPT-05 Be-10 quartz 2.501e+05 5.725e+03 07KNSTD;
05-PPT-05 Be-10 quartz 2.748e+05 7.983e+03 07KNSTD;
05-PPT-08 41.26379 -112.47476 1606 std  2.5 2.68 0.9860 0.00e+00 2005;
05-PPT-08 true_t PPT 18300 300;
05-PPT-08 Be-10 quartz 2.536e+05 3.512e+03 07KNSTD;
05-PPT-08 Be-10 quartz 2.474e+05 4.206e+03 07KNSTD;
```

```
05-PPT-08 Be-10 quartz 2.458e+05 6.143e+03 07KNSTD;
05-PPT-08 Be-10 quartz 2.892e+05 4.814e+03 KNSTD;
05-PPT-08 Be-10 quartz 2.480e+05 4.429e+03 07KNSTD;
05-PPT-08 Be-10 quartz 2.734e+05 7.901e+03 07KNSTD;
HU08-01 -13.94494 -70.89539 4854 std  7.0 2.29 0.9969 8.20e-04 2008;
HU08-01 true_t HUANCANE2A 12200 560;
HU08-01 Be-10 quartz 4.949e+05 9.314e+03 07KNSTD;
HU08-01 Be-10 quartz 4.896e+05 1.013e+04 07KNSTD;
HU08-01 Be-10 quartz 5.241e+05 1.201e+04 07KNSTD;
HU08-01 Be-10 quartz 5.390e+05 1.011e+04 07KNSTD;
HU08-02 -13.94635 -70.89241 4862 std  5.0 2.29 0.9990 4.84e-04 2008;
HU08-02 true_t HUANCANE2A 12200 560;
HU08-02 Be-10 quartz 5.003e+05 1.022e+04 07KNSTD;
HU08-02 Be-10 quartz 4.946e+05 1.557e+04 07KNSTD;
HU08-02 Be-10 quartz 5.418e+05 1.018e+04 07KNSTD;
HU08-02 Be-10 quartz 5.195e+05 9.767e+03 07KNSTD;
HU08-03 -13.94613 -70.89266 4859 std  6.0 2.29 0.9947 3.20e-04 2008;
HU08-03 true_t HUANCANE2A 12200 560;
HU08-03 Be-10 quartz 4.835e+05 9.099e+03 07KNSTD;
HU08-03 Be-10 quartz 5.265e+05 9.883e+03 07KNSTD;
HU08-04 -13.94545 -70.89280 4848 std  5.0 2.29 0.9914 8.20e-04 2008;
HU08-04 true_t HUANCANE2A 12200 560;
HU08-04 Be-10 quartz 4.977e+05 7.205e+03 07KNSTD;
HU08-04 Be-10 quartz 4.883e+05 8.239e+03 07KNSTD;
HU08-04 Be-10 quartz 5.125e+05 9.632e+03 07KNSTD;
HU08-06 -13.94454 -70.89483 4843 std  7.0 2.29 0.9993 4.84e-04 2008;
HU08-06 true_t HUANCANE2A 12200 560;
HU08-06 Be-10 quartz 5.081e+05 9.569e+03 07KNSTD;
HU08-06 Be-10 quartz 4.992e+05 7.616e+03 07KNSTD;
HU08-06 Be-10 quartz 5.009e+05 9.418e+03 07KNSTD;
HU08-10 -13.94700 -70.88693 4860 std  3.2 2.29 0.9975 4.84e-04 2008;
HU08-10 true_t HUANCANE2A 12200 560;
HU08-10 Be-10 quartz 5.142e+05 1.286e+04 07KNSTD;
HU08-10 Be-10 quartz 5.012e+05 8.335e+03 07KNSTD;
HU08-10 Be-10 quartz 5.329e+05 1.001e+04 07KNSTD;
HU08-11 -13.94715 -70.88680 4860 std  6.0 2.29 0.9990 6.56e-04 2008;
HU08-11 true_t HUANCANE2A 12200 560;
HU08-11 Be-10 quartz 5.250e+05 8.751e+03 07KNSTD;
HU08-11 Be-10 quartz 5.147e+05 6.469e+03 07KNSTD;
HU08-14 -13.94887 -70.88559 4871 std  5.0 2.29 0.9960 3.20e-04 2008;
HU08-14 true_t HUANCANE2A 12200 560;
HU08-14 Be-10 quartz 5.138e+05 9.607e+03 07KNSTD;
HU08-14 Be-10 quartz 5.078e+05 8.451e+03 07KNSTD;
HU08-15 -13.94838 -70.88537 4869 std  6.0 2.29 0.9950 6.56e-04 2008;
HU08-15 true_t HUANCANE2A 12200 560;
HU08-15 Be-10 quartz 4.929e+05 9.240e+03 07KNSTD;
HU08-15 Be-10 quartz 4.385e+05 7.900e+03 07KNSTD;
HU08-16 -13.94679 -70.88619 4867 std  6.0 2.29 0.9974 3.20e-04 2008;
HU08-16 true_t HUANCANE2A 12200 560;
HU08-16 Be-10 quartz 5.151e+05 9.598e+03 07KNSTD;
HU08-16 Be-10 quartz 4.459e+05 8.500e+03 07KNSTD;
```

The ICE-D project now has a **partially complete documentation wiki**.

Questions about this page: **Greg Balco** or **Pierre-Henri Blard**

Table S1. Effective vertical cutoff rigidity (R_c) and corresponding magnetic scaling factor ($f(R_c)$) as a function of latitude for various geomagnetic field models.

	R_c (GV)				$f(R_c)$			
Lat |°|	GAD	SHA	K27	TK03	GAD	SHA	K27	TK03
0	14.745	14.665	14.197	14.347	0.538	0.540	0.551	0.548
1	14.743				0.538			
2	14.735				0.539			
3	14.723				0.539			
4	14.705				0.539			
5	14.681	14.556	14.081	14.247	0.540	0.543	0.554	0.550
6	14.650				0.541			
7	14.612				0.541			
8	14.565				0.543			
9	14.509				0.544			
10	14.444	14.234	13.716	13.946	0.545	0.550	0.563	0.558
11	14.366				0.547			
12	14.277				0.549			
13	14.174				0.552			
14	14.057				0.555			
15	13.924	13.619	13.083	13.365	0.558	0.566	0.580	0.572
16	13.775				0.562			
17	13.610				0.566			
18	13.426				0.571			
19	13.225				0.576			
20	13.005	12.632	12.172	12.581	0.582	0.592	0.605	0.594
21	12.766				0.588			
22	12.509				0.596			
23	12.233				0.603			
24	11.939				0.612			
25	11.627	11.252	10.997	11.391	0.621	0.633	0.641	0.629
26	11.299				0.632			
27	10.955				0.642			
28	10.597				0.654			
29	10.226				0.667			
30	9.843	9.542	9.608	9.915	0.680	0.691	0.689	0.678
31	9.450				0.694			
32	9.049				0.709			
33	8.643				0.725			
34	8.232				0.742			
35	7.819	7.653	8.090	8.319	0.759	0.766	0.748	0.738
36	7.406				0.777			
37	6.995				0.795			
38	6.589				0.813			
39	6.189				0.832			
40	5.797	5.783	6.551	6.781	0.850	0.851	0.815	0.804
41	5.414				0.868			
42	5.044				0.886			
43	4.686				0.902			
44	4.343				0.918			
45	4.016	4.122	5.097	5.464	0.933	0.928	0.883	0.866

46	3.704				0.946			
47	3.410				0.958			
48	3.133				0.968			
49	2.874				0.976			
50	2.633	2.792	3.813	4.172	0.983	0.978	0.941	0.926
51	2.409				0.988			
52	2.202				0.992			
53	2.011				0.995			
54	1.836				0.997			
55	1.676	1.817	2.747	3.298	0.998	0.997	0.980	0.962
56	1.528				0.999			
57	1.393				0.999			
58	1.269				1.000			
59	1.155				1.000			
60	1.049	1.137	1.910	2.591	1.000	1.000	0.996	0.984
61	0.951				1.000			
62	0.858				1.000			
63	0.771				1.000			
64	0.688				1.000			
65	0.608	0.659	1.280	1.884	1.000	1.000	1.000	0.996
66	0.532				1.000			
67	0.458				1.000			
68	0.386				1.000			
69	0.318				1.000			
70	0.252	0.328	0.828	1.506	1.000	1.000	1.000	0.999
71	0.191				1.000			
72	0.133				1.000			
73	0.081				1.000			
74	0.036				1.000			
75	-0.003	0.122	0.518	1.088	1.000	1.000	1.000	1.000
76	-0.032				1.000			
77	-0.053				1.000			
78	-0.064				1.000			
79	-0.064				1.000			
80	-0.054	0.026	0.322	0.906	1.000	1.000	1.000	1.000
81	-0.034				1.000			
82	-0.006				1.000			
83	0.029				1.000			
84	0.066				1.000			
85	0.102	0.002	0.215	0.770	1.000	1.000	1.000	1.000
86	0.131				1.000			
87	0.145				1.000			
88	0.136				1.000			
89	0.092				1.000			
90	0.000	0.000	0.180	0.773	1.000	1.000	1.000	1.000

GAD is mean effective vertical cutoff rigidity (R_c, in GV) as a function of absolute latitude (Lat) at sea level calculated using Equation 2 of Lifton et al. (2014); SHA is mean R_c for VGP distribution calculated from dipole coefficients for 14 cal. ka to present from Pavón-Carrasco et al. (2014); K27 is mean R_c for VGP distribution with Fisher's precision parameter K=27; and TK03 is mean R_c for the statistical geomagnetic field model of Tauxe and Kent (2004). The corresponding magnetic scaling factors ($f(R_c)$) were calculated with mean R_c using Equation 6 with Dorman function in Desilets et al. (2006). Mean and standard deviation (SD) are for GAD, SHA, K27, and TK03 entries for R_c and for $f(R_c)$.